nature electronics

SUPPLEMENTARY INFORMATION

https://doi.org/10.1038/s41928-019-0287-1

In the format provided by the authors and unedited.

Graphene ribbons with suspended masses as transducers in ultra-small nanoelectromechanical accelerometers

Xuge Fan[1*], Fredrik Forsberg[2], Anderson D. Smith[3], Stephan Schröder[1,4], Stefan Wagner[5], Henrik Rödjegård[4], Andreas C. Fischer[1,6], Mikael Östling[3], Max C. Lemme[3,5,7*] and Frank Niklaus[1*]

[1]Department of Micro and Nanosystems, School of Electrical Engineering and Computer Science, KTH Royal Institute of Technology, Stockholm, Sweden. [2]Scania Technical Centre, Södertälje, Sweden. [3]Department of Integrated Devices and Circuits, School of Electrical Engineering and Computer Science, KTH Royal Institute of Technology, Kista, Sweden. [4]Senseair AB, Delsbo, Sweden. [5]AMO GmbH, Aachen, Germany. [6]Silex Microsystems AB, Järfälla, Sweden. [7]Chair of Electronic Devices, Faculty of Electrical Engineering and Information Technology, RWTH Aachen University, Aachen, Germany.
*e-mail: xuge@eecs.kth.se; lemme@amo.de; frank.niklaus@eecs.kth.se

SUPPLEMENTARY INFORMATION

CONTENTS

S1. Double-layer graphene transfer process

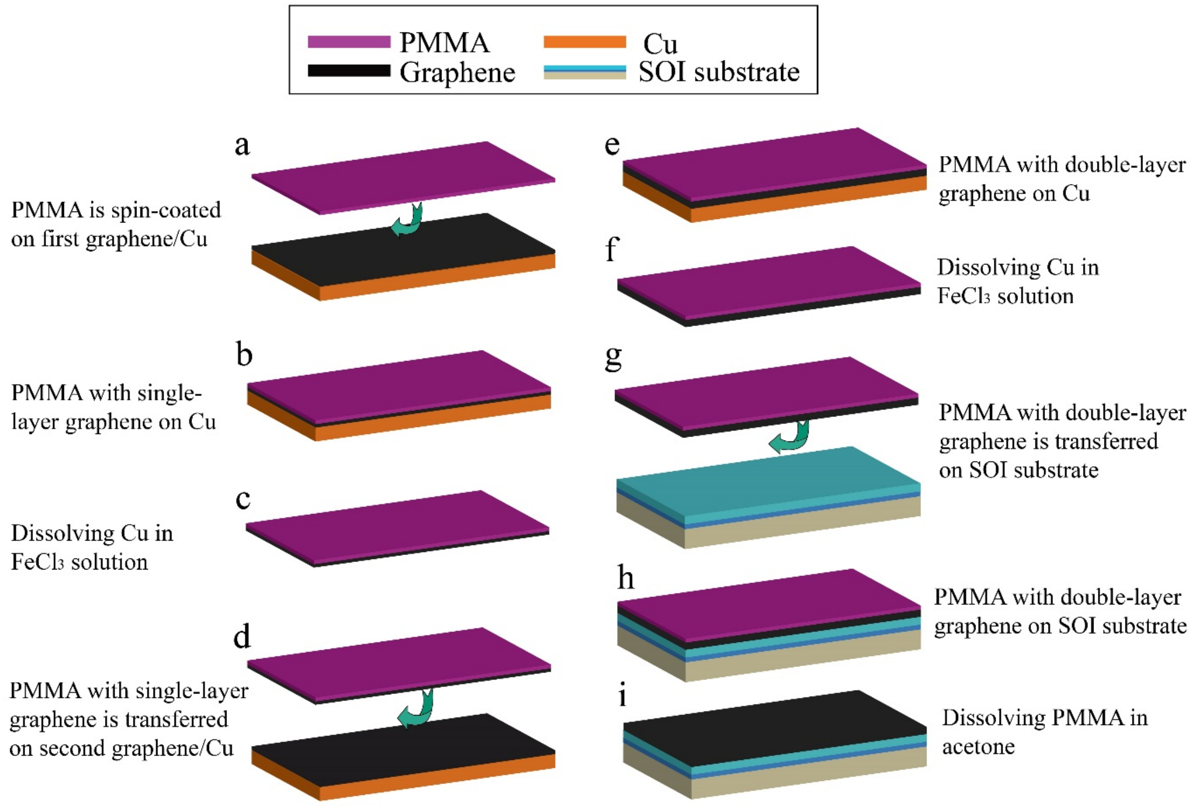

Figure S1| Schematic of double-layer graphene transfer process. **a**, CVD-grown single-layer graphene on a copper foil that is coated with a 200 nm thick layer of PMMA. **b**, PMMA on graphene and copper. **c**, Dissolving the copper in $FeCl_3$. **d,** Transferring 1st PMMA/graphene stack of **c** to 2nd CVD-grown single-layer graphene on copper foil using a transfer process. **e,** PMMA with double-layer graphene on copper. **f**, Dissolving the copper in $FeCl_3$. **g**, Transfer of PMMA with double-layer graphene to pre-patterned SOI substrate. **h**. PMMA and double-layer graphene on the top of SiO_2 layer on SOI substrate. **i**, Dissolving PMMA firstly in acetone.

S2. Device characterization using optical microscopy, SEM imaging and Raman spectroscopy

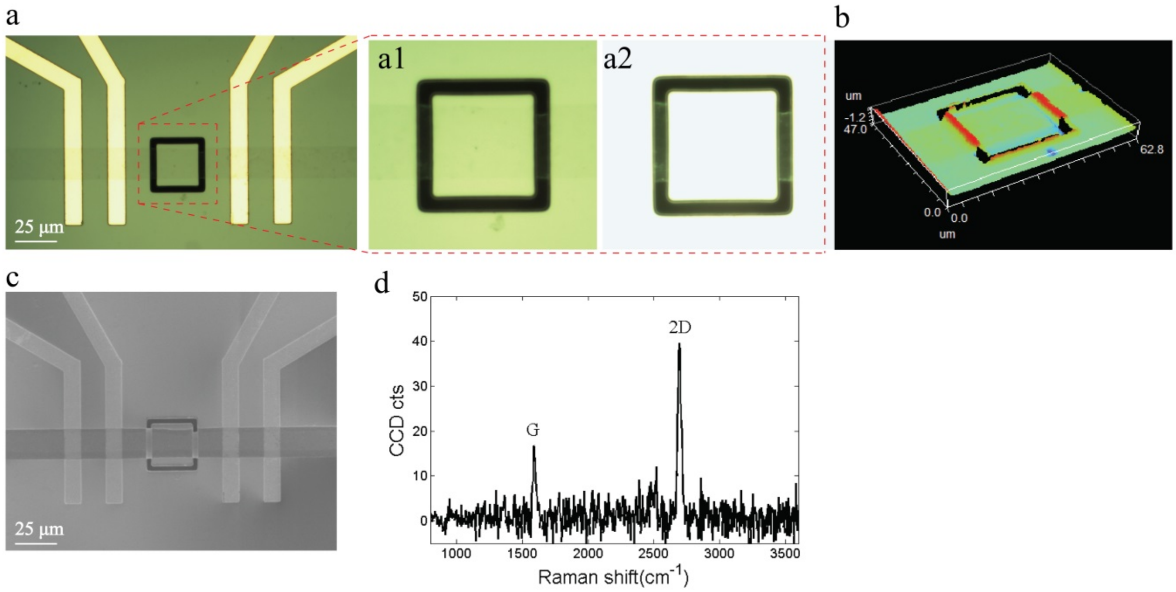

Figure S2| Device characterization with optical microscopy, SEM imaging and Raman spectroscopy. **a**, Optical microscope images of a device with dimensions of the proof mass of 25 µm × 25 µm × 16.4 µm, graphene ribbon width of 18 µm, and length of the suspended graphene ribbons (trench width) of 2 × 3 µm. **a1**, High magnification microscope image of silicon proof mass attached to the suspended double-layer graphene ribbons. **a2**, High-contrast microscope image of the device in **a1** with adjusted light intensity. The graphene ribbons can be clearly observed. **b**, 3D plot of the device from **a** using white light interferometry. **c**, Corresponding SEM image. **d**, Raman spectroscopy of suspended double-layer graphene in a device. The characteristic "G-peak" occurring at around 1586.9 cm^{-1} and the "2D-peak" occurring at around 2694.5 cm^{-1} demonstrate the presence of graphene.

S3. Characterization using white light interferometry to verify release and static deflection of the proof masses

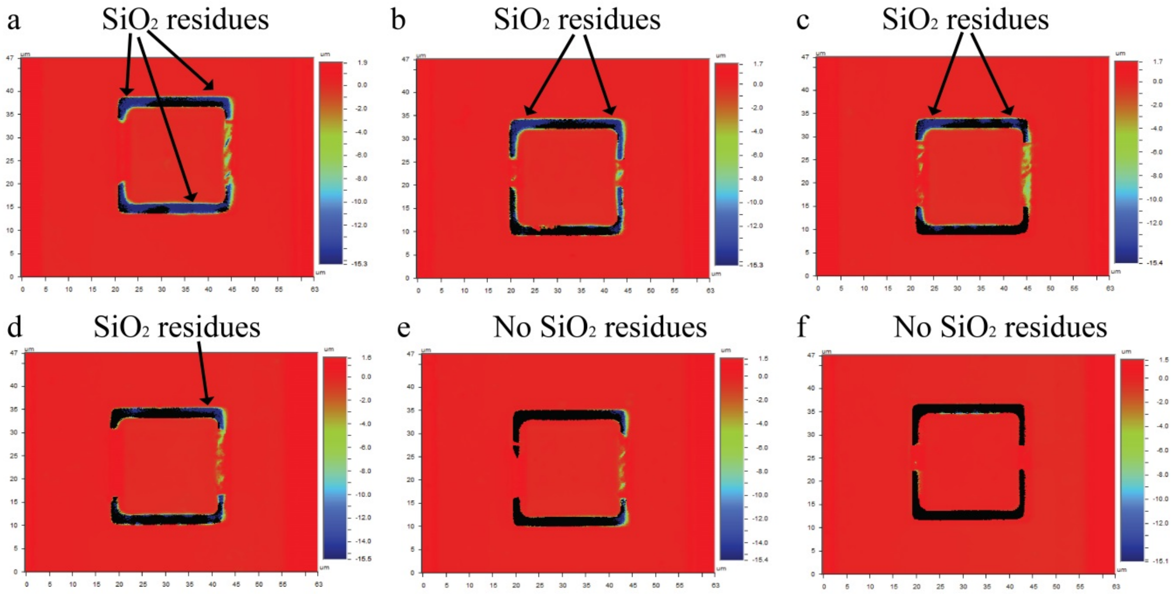

Figure S3| Demonstration of release of the proof masses using white light interferometry. The release of the silicon proof masses after vapour HF etching was confirmed using white light interferometry by imaging to a depth of 17 µm below the substrate surface. In this way residues of the BOX (SiO_2) layer in the trenches became visible. **a-c**, SiO_2 residues (dark blue colour) that partly connect the silicon proof mass with the handle substrate, are visible in the trenches, showing that these proof masses are not fully released. **d**, SiO_2 residues (dark blue colour) are remaining, however they are not connected to the silicon proof mass. **e-f**, No SiO_2 residues are left (no dark blue colour), confirming that the silicon proof mass is fully released.

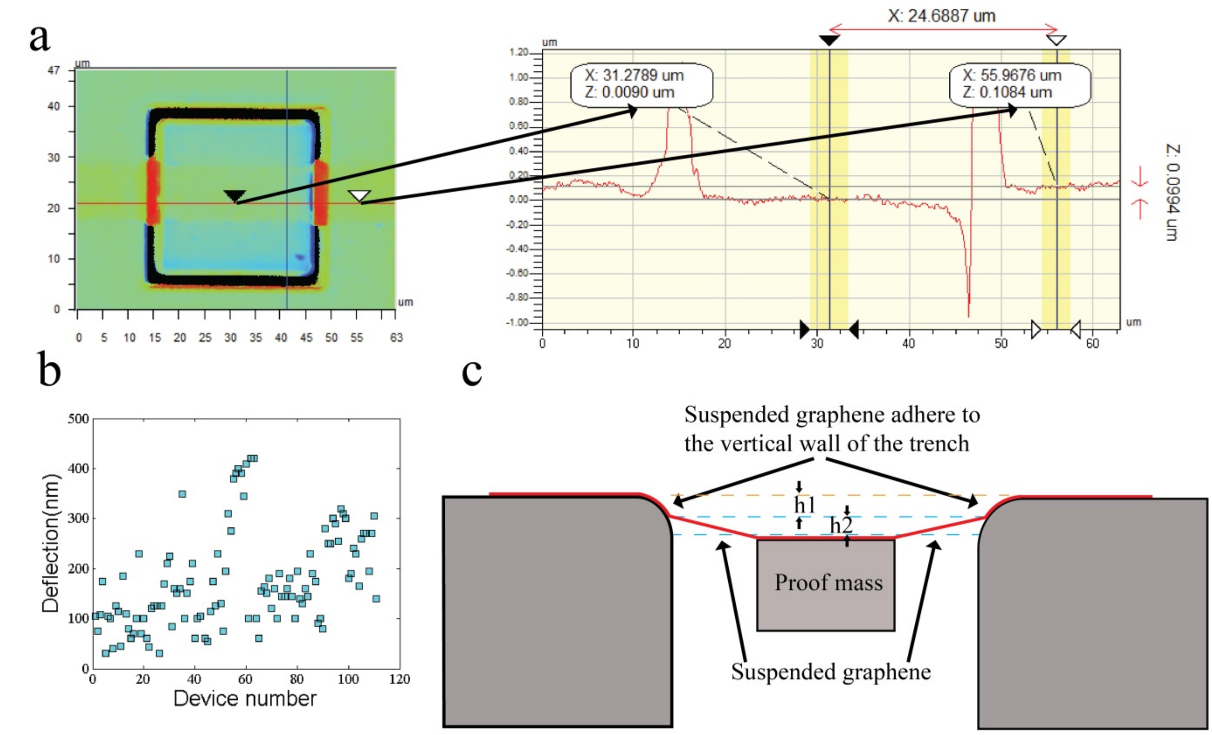

Figure S4| Measurement of static displacement of the released proof masses in relation to the substrate surface using white light interferometry. **a**, Measurement of the top SiO_2 surface of a device with silicon proof mass dimensions of 30 µm × 30 µm × 16.4 µm, a graphene ribbon width of 13 µm, and a length of the graphene ribbons (trench width) of 2 × 3 µm. It can be seen that the graphene ribbons with the suspended proof mass is deflected downwards. The static displacement of the proof mass below the device surfaces is approximately 100 nm in this device. **b**, Static displacement of released proof masses in 110 different devices, with different trench widths, graphene ribbon widths and dimensions of the poof masses. **c**, Cross-sectional schematic illustrating the static displacement of a proof mass in a device with microscopically rounded edges. The adhesion between the graphene and the SiO_2 surfaces of the substrate and the proof mass is due to van der Waals forces[6, 36].

S4. Electrical characterization of the patterned graphene

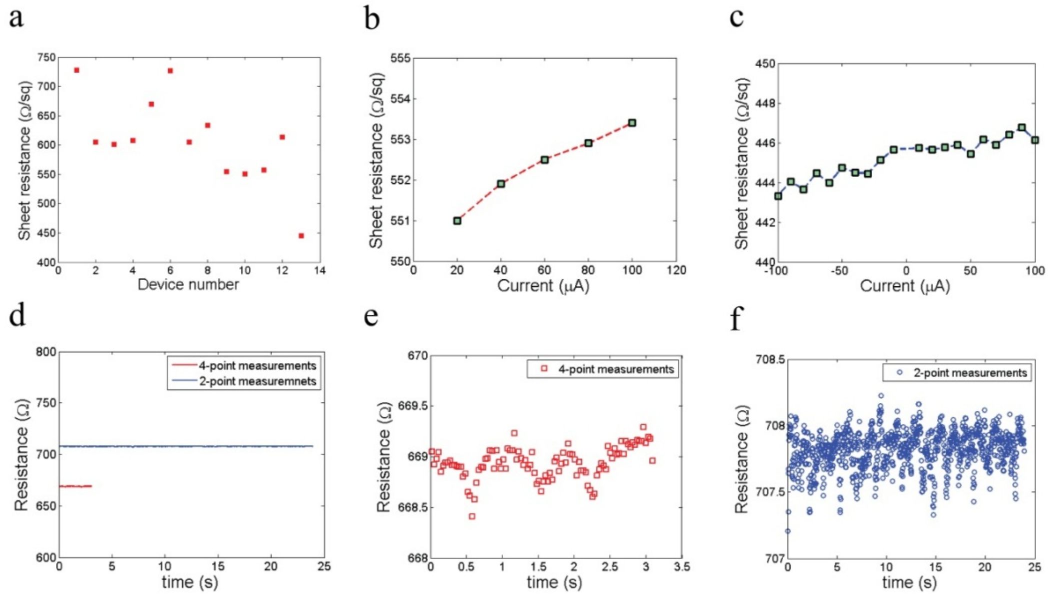

Figure S5| Electrical characterization of the patterned graphene. **a**, Sheet resistance of double-layer graphene measured by four-point measurements in 100 μA current sweeping mode of 13 devices. The sheet resistance of the double-layer graphene typically is in the range between 500-700 Ω/sq. **b**, Sheet resistance measurements of device 10 from **a,** at current sweeping mode from 20 μA to 100 μA with steps of 20 μA. The sheet resistance is reasonably stable, with a slight increase of the sheet resistance for increasing currents caused by current heating. **c**, Sheet resistance measurements of device 13 from **a** at current sweeping mode from -100 μA to 100 μA with steps of 10 μA. The sheet resistance is reasonably stable, with a slight increase of the sheet resistance for increasing currents caused by current heating. **d**, Comparison of the resistance of the double-layer graphene ribbon of device 5 from **a**. The device is wire bonded and measured by two-point and four-point measurements with a sampling current of 50 μA. The results confirm a good contact resistance of about 40 Ω between the graphene patch and the gold electrodes. **e**, Data points from 100 measurements over time using 4-point measurements of **d**. **f**, Data points from 1000 measurements over time using two-point measurements of **d**. Double-layer graphene resistance variations of about 0.5 Ω over long time intervals (seconds).

S5. Summary of devices and device dimensions

TABLE S1. Dimensions of the characterized devices.

Dimensions / Devices	Proof mass dimensions (width × length × height) (μm^3)	Total combined length of the two suspended graphene ribbons (µm)	Graphene ribbon width (µm)	Notes
Device 1	20 × 20 × 16.4	6	13.5	
Device 2	30 × 30 × 16.4	6	13	
Device 3	30 × 30 × 16.4	6	24	
Device 4	25 × 25 × 16.4	4	10	Proof mass centre line is placed ~2 µm beside the centre line of the ribbons.
Device 5	30 × 30 × 16.4	6	7	
Device 6	15 × 15 × 16.4	8	5	Proof mass centre line is placed ~4 µm beside the centre line of the ribbons.
Device 7	20 × 20 × 16.4	6	14	One of the two suspended ribbons contains a defect (hole).
Device 8	20 × 20 × 16.4	8	6	
Device 9	20 × 20 × 16.4	8	10	
Device 10	25 × 25 × 16.4	6	6	
Device 11	25 × 25 × 16.4	6	10	
Device 12	40 × 40 × 16.4	8	8	
Device 13	40 × 40 × 16.4	8	5	
Device 14	40 × 40 × 16.4	8	20	
Device 15	40 × 40 × 16.4	8	20	
Device 16	50 × 50 × 16.4	4	44	
Device 17	25 × 25 × 16.4	6	17	
Device 18	40 × 40 × 16.4	4	34	
Device 19	40 × 40 × 16.4	6	20	
Device 20	50 × 50 × 16.4	4	15	

S6. Comparison of suspended graphene structures with attached masses

TABLE S2. Comparison of suspended graphene membranes or ribbons with attached masses reported in literature.

Author	Material(s) of mass	Shape of mass	Side length (μm^2) or diameter (μm)	Thickness (μm)	Area (μm^2)	Volume (μm^3)	Density (g/cm^3)	Mass (g)
Present work	Silicon/SiO_2	Cube	50 × 50	SiO_2: 1.4	2500	SiO_2: 3500	2.2	0.95×10^{-7}
				Silicon: 15		Silicon: 37500	2.329	
Hurst[18]	SU-8	Cylinder	10	1.5	78.5	117. 75	1. 199	1.41×10^{-10}
Blees[19]	Gold	Thin film	10 × 10	0.05	100	5	19.3	9.65×10^{-13}
Matsui[20]	Carbon	Thin film	0.5 × 1.5	0.02	0.75	0. 015	3.8	5.7×10^{-14}

S7. Comparison of proof mass dimensions and sizes, and normalized relative resistance changes of reported MEMS accelerometers

TABLE S3. Comparison of proof mass dimensions and sizes of piezoresistive and capacitive accelerometers.

Author	Material	Type	Die area occupied by proof mass (μm^2)	Die area occupied by functional device parts (μm^2)	Volume of proof mass (μm^3)	Mass of proof mass (g)
Present work (device 1)	Graphene	piezoresistive	4×10^2	$\sim 4.8 \times 10^3$	6.56×10^3	1.55×10^{-8}
Wung[44]	Silicon	piezoresistive	2.4×10^5	$> 2.4 \times 10^5$	9.6×10^7	2.27×10^{-4}
Kavitha[59]	Silicon	piezoresistive	2.7×10^7	$> 2.7 \times 10^7$	2.33×10^{10}	5.5×10^{-2}
Roy[46]	Silicon	piezoresistive	1.23×10^7	$> 1.23 \times 10^7$	8.27×10^9	1.95×10^{-2}
Roy[60]	Silicon	piezoresistive	4.84×10^6	$> 4.84 \times 10^6$	3.27×10^9	7.73×10^{-3}
Zhang[47]	Silicon	piezoresistive	5.24×10^5	$> 5.24 \times 10^5$	2.62×10^7	6.2×10^{-5}
Haris[61]	poly silicon	piezoresistive	2.5×10^5	$> 2.5 \times 10^5$	1×10^7	2.37×10^{-5}
Kal[62]	Silicon	piezoresistive	1.23×10^7	$> 1.23 \times 10^7$	3.43×10^9	8.1×10^{-3}
Plaza[48]	Silicon	piezoresistive	8.1×10^6	$> 8.1 \times 10^6$	3.65×10^9	8.62×10^{-3}
ADXL 05 (commercial)	Silicon	capacitive	$\sim 2.9 \times 10^4$	$\sim 1.93 \times 10^5$	5.8×10^4	1.35×10^{-7}
Ma[63]	Silicon	capacitive	5.2×10^6	$> 5.2 \times 10^6$	1.3×10^9	$\sim 3\times 10^{-3}$
Junseok[64]	Silicon	capacitive	2.4×10^6	$> 2.4 \times 10^6$	1.14×10^9	2.65×10^{-3}
Zhou[65]	Silicon	capacitive	7.3×10^5	$> 7.3 \times 10^5$	2.92×10^7	6.81×10^{-5}
Aydin[66]	Silicon	capacitive	4.66×10^6	1.06×10^7	1.63×10^8	3.8×10^{-4}
Sun[67]	Silicon	capacitive	1.71×10^6	$> 1.71 \times 10^6$	8.58×10^7	2×10^{-4}
Amini[68]	Silicon	capacitive	1.2×10^7	$> 1.2 \times 10^7$	4.8×10^8	1.2×10^{-3}

TABLE S4. Comparison of the relative resistance change per proof mass volume of different piezoresistive accelerometers reported in literature.

<table>
<tr><th>Author</th><th>Year</th><th>Dimensions and volume of proof mass (width × length × height) (μm^3)</th><th>Output voltage prior to signal amplification at applied 1 g acceleration</th><th>Relative resistance change ($\Delta R/R$) prior to signal amplification at applied 1 g acceleration</th><th colspan="2">Relative resistance change ($\Delta R/R$) per proof mass volume ($\frac{\Delta R/R}{V}$) prior to signal amplification applied 1 g acceleration (μm^{-3})</th><th>Spring and strain gauge materials</th></tr>
<tr><td rowspan="4">Present work (device1)</td><td rowspan="4">2019</td><td rowspan="4">20 × 20 × 16.4 = 6.56×10^3</td><td rowspan="4">4.1 μV/100μA</td><td>$\Delta R/R_{SG}$**</td><td>($\frac{\Delta R/R_{SG}}{V}$)</td><td>($\frac{\Delta R/R_{SG}}{V}$)/30*</td><td rowspan="4">graphene</td></tr>
<tr><td>1.88×10^{-4}</td><td>3.13×10^{-8}</td><td>1.04×10^{-9}</td></tr>
<tr><td>$\Delta R/R$**</td><td>($\frac{\Delta R/R}{V}$)</td><td>($\frac{\Delta R/R}{V}$)/30*</td></tr>
<tr><td>2.73×10^{-5}</td><td>4.16×10^{-9}</td><td>1.39×10^{-10}</td></tr>
<tr><td>Kavitha[59] ***</td><td>2016</td><td>5200 × 5200 × 860 = 2.33×10^{10}</td><td>4 mV/V</td><td>4×10^{-3}</td><td colspan="2">1.72×10^{-13}</td><td>silicon</td></tr>
<tr><td>Wung[44]</td><td>2015</td><td>400 × 600 × 400 = 9.6×10^7</td><td>3.0015 μV/V</td><td>6×10^{-7}</td><td colspan="2">6.25×10^{-15}</td><td>silicon</td></tr>
<tr><td>Roy[46]</td><td>2015</td><td>3500 × 3500 × 675 = 8.27×10^9</td><td>20 μV/350 μA</td><td>1.84×10^{-5}</td><td colspan="2">2.23×10^{-15}</td><td>silicon</td></tr>
<tr><td>Roy[60] ****</td><td>2014</td><td>2200 × 2200 × 675 = 3.27×10^9</td><td>4 mV/V</td><td>4×10^{-3}</td><td colspan="2">1.22×10^{-12}</td><td>silicon</td></tr>
<tr><td>Zhang[47]</td><td>2014</td><td>Fan-shaped: 1mm radius, 50 μm height, 60° angle = 2.62×10^7</td><td>0.155 mV/V</td><td>6.2×10^{-4}</td><td colspan="2">2.37×10^{-11}</td><td>silicon</td></tr>
<tr><td>Haris[61] ***</td><td>2010</td><td>500 ×500 ×40 = 10^7</td><td>0.077mV</td><td>4.26×10^{-4}</td><td colspan="2">6.53×10^{-12}</td><td>poly silicon</td></tr>
<tr><td>Kal[62] ****</td><td>2006</td><td>3500×3500×280 = 3.43×10^9</td><td>0.506 mV</td><td>5.06×10^{-4}</td><td colspan="2">1.48×10^{-13}</td><td>silicon</td></tr>
<tr><td>Plaza[48]</td><td>2002</td><td>2700×3000×450 = 3.65×10^9</td><td>0.43 mV</td><td>4.3×10^{-4}</td><td colspan="2">1.18×10^{-13}</td><td>silicon</td></tr>
</table>

* As discussed in the paper, the effective acceleration acting on the suspended proof mass may be significantly higher than the 1 g acceleration measured by the reference accelerometer of the shaker due to vibration modes of that do not belong to the spring-mass system of the device. According to the analysis, it is possible that the effective acceleration levels at the proof mass may reach up to 20-30 g at an applied acceleration of 1 g. Therefore, we reduced the values for the relative resistance change per proof mass volume in our devices by a factor of 30 times to obtain a fair and conservative comparison to other devices.

** R is the total resistance of a graphene device while R_{SG} is the total resistance of the suspended graphene ribbons.

*** The values are based on simulation results.

****Because no amplification factor was provided, we assumed an amplification factor of 1.

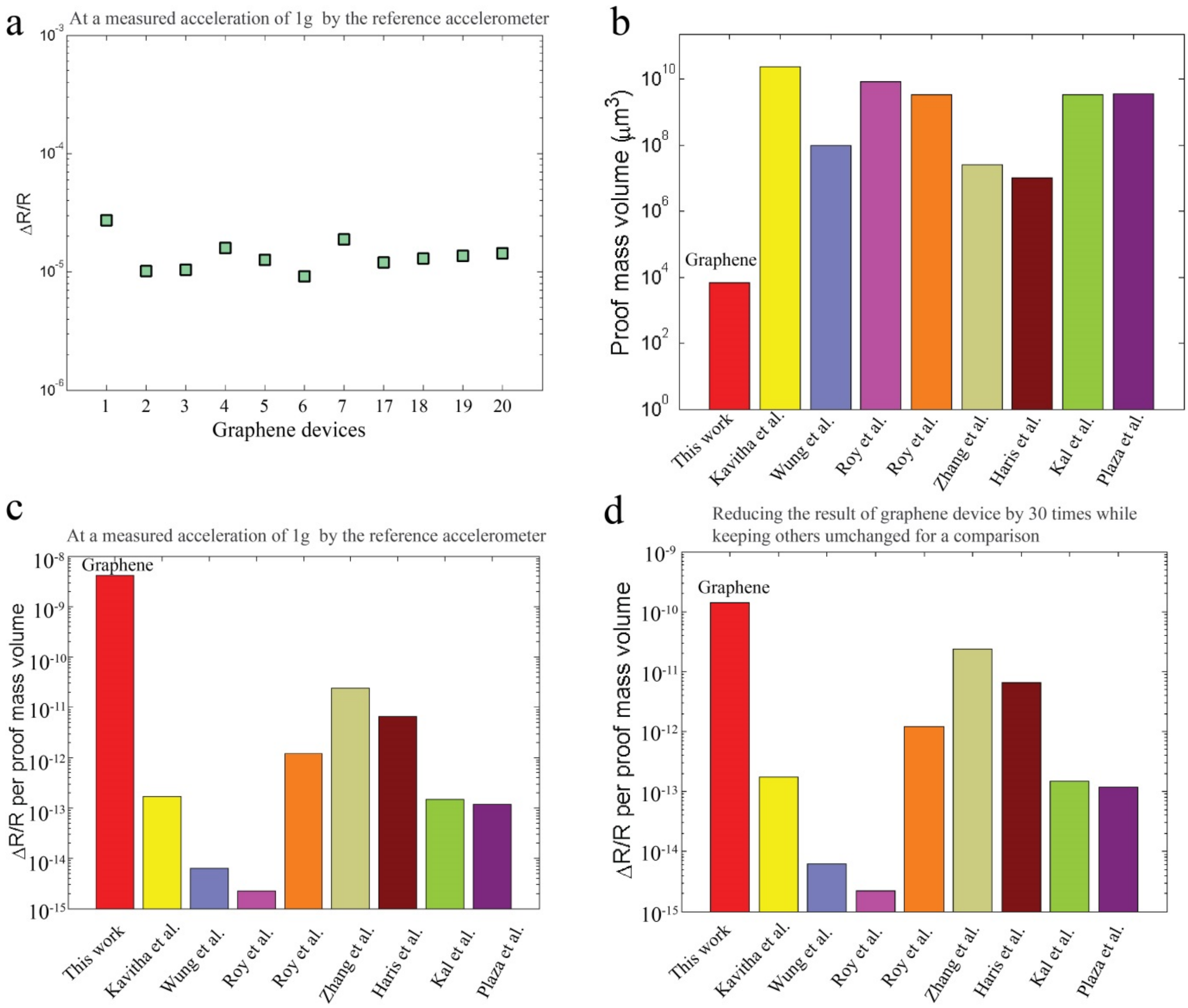

Figure S6 | Signal response of graphene devices and piezoresistive accelerometers reported in literature (y-axis, log plot). **a,** Plot of relative resistance change (ΔR/R) of measured graphene devices for an acceleration of 1 g at a frequency of 160 Hz as measured by the reference accelerometer of the shaker **b,** Comparison of the proof mass volume of graphene device 5 with other silicon piezoresistive accelerometers reported in literature[44,46-48,59-62]. **c** and **d,** Comparison of relative resistance change per proof mass volume of graphene device 5 and other piezoresistive silicon-based accelerometers reported in literature, indicating that the relative resistance change per proof mass volume of graphene accelerometers is at least one order of magnitude larger than that of conventional silicon accelerometers[44, 46-48, 59-62], even though we exclude a possible amplification of the acceleration (30x) in our measurements due to resonance effects (**d**). Tabulated values are provided in Table S4.

S8. Measurement circuit and experimental setup for device characterization and measurements

The total resistance of a graphene ribbon is the input resistance in the measurement circuit supplied with an adjustable DC current (30-100 μA) as shown in Figure S7a. If the proof mass is displaced, the resistance of the two suspended graphene ribbons changes due to the piezoresistivity of graphene. The changes in the output voltage caused by the change of the graphene resistance is read by a first-order high-pass filter with a cut-off frequency of 0.079 Hz, amplified by an amplifier (LT1001OP, Linear Technology), read by another external first-order high-pass filter with a cut off frequency of 15 Hz, recorded by a dynamic signal analyser (HP 35670A), and finally recorded through the computer interface.

The packaged graphene device chip and the electronic measurement circuit were encapsulated in a shielding box (Figure S7b-d), which was placed onto an air-bearing shaker (PCB 396c11, The Modal Shop) with a build-in high-precision reference accelerometer. Coaxial cables were connecting the measurement circuit inside the shielding box to a spectrum analyser. An adjustable DC input current (30-100 μA) was produced by using a DC stabilized voltage supply in combination with resistors. The air-bearing shaker and the dynamic signal analyser are controlled through a computer interface to apply accelerations at defined frequencies and to read out the sensing signal in form of the output voltage. A sine wave excitation signal was used to excite the air-bearing shaker.

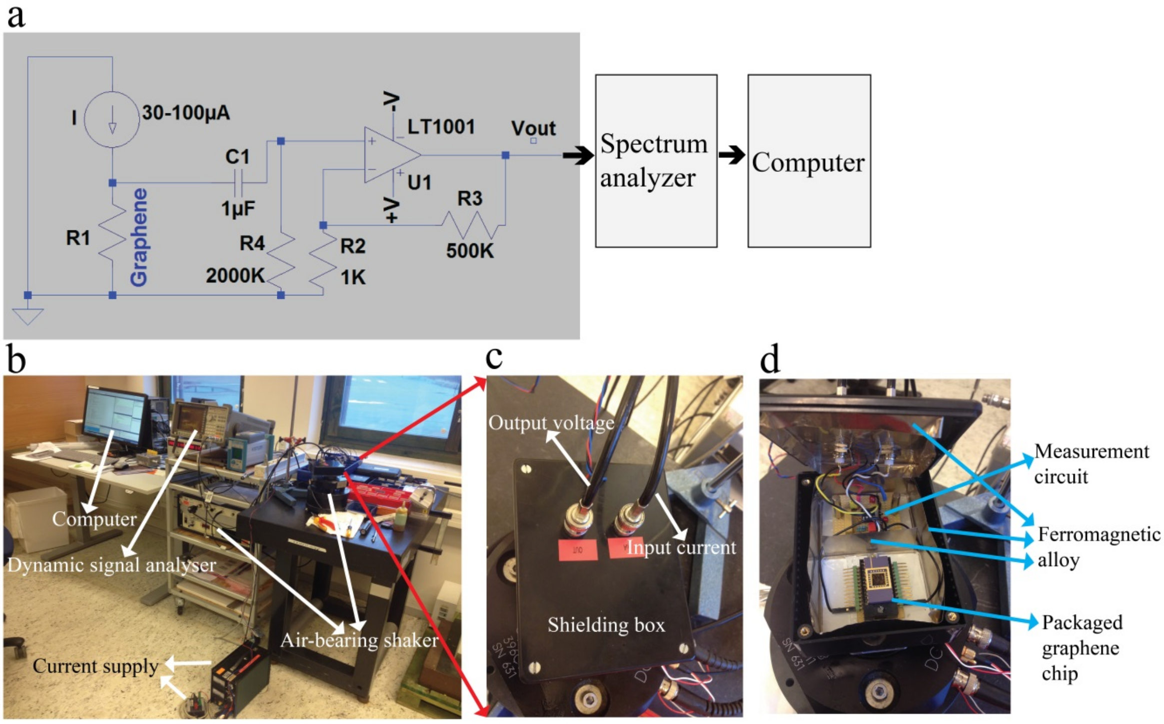

Figure S7| Measurement circuit and experimental setup. **a**, Schematic of the measurement circuit and the data acquisition setup. **b**, Photograph of the measurement setup. **c**, Shielding box including the packaged graphene devices and measurement circuit with a signal amplification of a factor of 500, placed on the air-bearing shaker. **d**, View inside the shielding box that is providing electrostatic and magnetic shielding. A foil consisting of a ferromagnetic alloy was used in the box to shield the devices and the measurement circuit towards outside electric and magnetic fields, and to separate the graphene devices from the measurement circuit, thereby effectively reducing crosstalk.

S9. Reference device and control measurements

A reference device was used to verify if possible influences of external environmental factors, such as humidity or parasitic electromagnetic signals induced in the graphene, have a significant influence on the output signals of the graphene devices. The reference device consisted of a graphene strip that is similar to the ones in the accelerometer devices, but without etched trenches in the underlying substrate surface (Fig. 2d). When exposed to an acceleration of 1 g at a frequency of 160 Hz as measured by the reference accelerometer, the output signal of the reference device is on the order of ~0.05 mV, which is about 40 times smaller than the output signal of ~2 mV of device 1 (Figure S8). The measurements of the reference device confirm that environmental factors do not have a significant impact on the output signal of the devices.

It is critically important to carefully shield the graphene devices and the measurement circuit from electric and magnetic fields, which was done in our experiments by encapsulating the devices and the measurement circuit in a shielding box that is covered on the inside with a foil made of a high-performance ferromagnetic alloy[69]. Likewise, the same foil is used to separate the graphene devices from the measurement circuit inside the shielding box (Figure S7d). To ensure and confirm that we have achieved proper shielding of the devices we have performed a number of control measurements of functional graphene devices and reference devices placed in the shielding box on the shaker. These control measurements included:

1) The shaker is not vibrating and there are no electrical connections to the measurement circuit and the graphene device (no acceleration, no measurement current).
2) The shaker is not vibrating but there are electrical connections to the measurement circuit and the graphene device (no acceleration, measurement current).
3) The shaker is vibrating but there are no electrical connections to the measurement circuit and the graphene device (acceleration acting on device, no measurement current).
4) The shaker is vibrating and there are electrical connections to the measurement circuit and the graphene device (regular measurement situation with acceleration acting on the device, measurement current).
5) The shaker is vibrating and there are electrical connections to the measurement circuit, but the shielding box is not mounted on / not in mechanical contact with the shaker (vibrating shaker but acceleration not acting on the device, measurement current).

The results from our control measurements showed that in the cases of 1), 2), 3) and 5) we measured no significant output signals, which is in contrast to the regular measurement situation in case 4). This confirmed that there were no magnetic or electric fields inside the box that caused significant noise signals or carrier conductivity modulation in the graphene transducer elements.

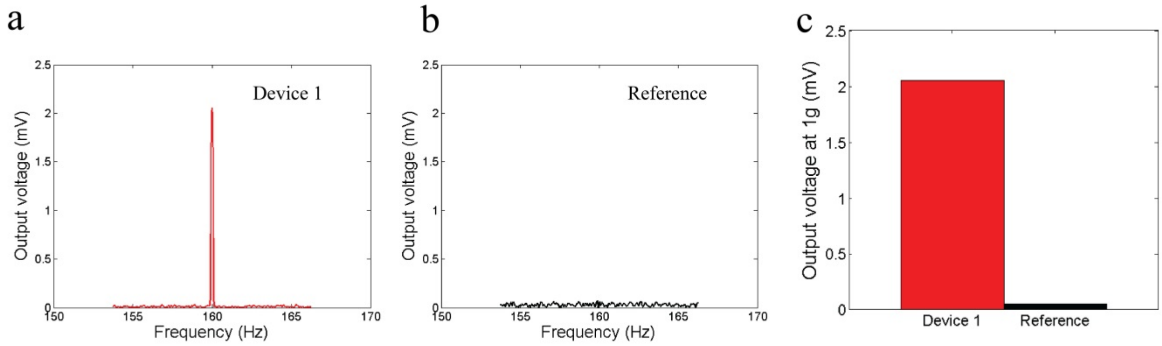

Figure S8| Control measurements. **a**, Measured spectrum of the output voltage of device 1 at an applied acceleration of 1 g at a frequency of 160 Hz as measured by the reference accelerometer of the shaker. For device 1 the dimensions of the proof mass are 20 µm × 20 µm × 16.4 µm, the ribbon width is 13.5 µm, and each of the two graphene ribbons is 3 µm long. **b**, Measured spectrum of the output voltage of a reference device at an applied acceleration of 1 g at a frequency of 160 Hz as measured by the reference accelerometer of the shaker. **c**, Comparison of the output voltages of device 1 and the reference device.

S10. Noise spectral density and resolution

Figure S9a, c and e show the measured output voltage of devices 1, 4 and 16 at the applied acceleration of 1 g at a frequency of 160 Hz as measured by the reference accelerometer of the shaker. Figure S9b, d and f show the measured noise spectral density (log-log plot) of devices 1, 4 and 16 respectively. The noise densities of the graphene devices were directly measured with a spectrum analyser (HP 35670A) in the frequency range from 16 Hz to 1600 Hz at an input current of 100 μA, while the shaker was not vibrating. The measured noise densities were in the range from 10^{-7} to 10^{-8} V/ √ Hz for devices 1 and 16, and 10^{-6} to 10^{-7} V/ √ Hz for device 4, illustrating that the 1/f-noise in these devices is comparably moderate. This is in agreement with the reported relatively low 1/f-noise of graphene patches[24-26]. It was reported[26] that the 1/f-noise in bilayer graphene typically is lower than in single-layer graphene and that the 1/f-noise reduction in bilayer graphene is associated with its band structure that varies with the charge distribution between the two atomic planes, resulting in screening of the potential fluctuations owing to the external impurity charges. The poor performance of device 4 as compared to device 1 might be due to a higher 1/f-noise density of device 4, which may be attributed to variations in the graphene quality after graphene transfer as devices 1 and 4 were fabricated in different process runs. In addition, the variation of built in stress in the graphene ribbons among different devices is also expected to influence the output signals and final performance of the graphene devices. The detection resolution of a device is a function of the noise density and frequency characteristic. It can be estimated by the noise density of the device at a frequency of 100 Hz knowing that it has a 1/f characteristic. For instance, in our measurements, according to Figure S9a and b, the noise density of device 1 can be expressed as Noise (f) $\approx \frac{100 \times 10^{-9}}{2 \times 10^{-3}} \times \sqrt{\frac{100}{f}}$ g/ √ Hz. The resolution can be calculated by the Resolution (f) $\approx \sqrt{\int_{f_1}^{f_2} \text{Noise}\,(f)^2 df}$. Thus, the noise density of device 1 is estimated to be ~50 μg/ √ Hz at 100 Hz, limited by 1/f-noise. This corresponds to a resolution of the order of 0.68 mg in the frequency range from 16 to 100 Hz.

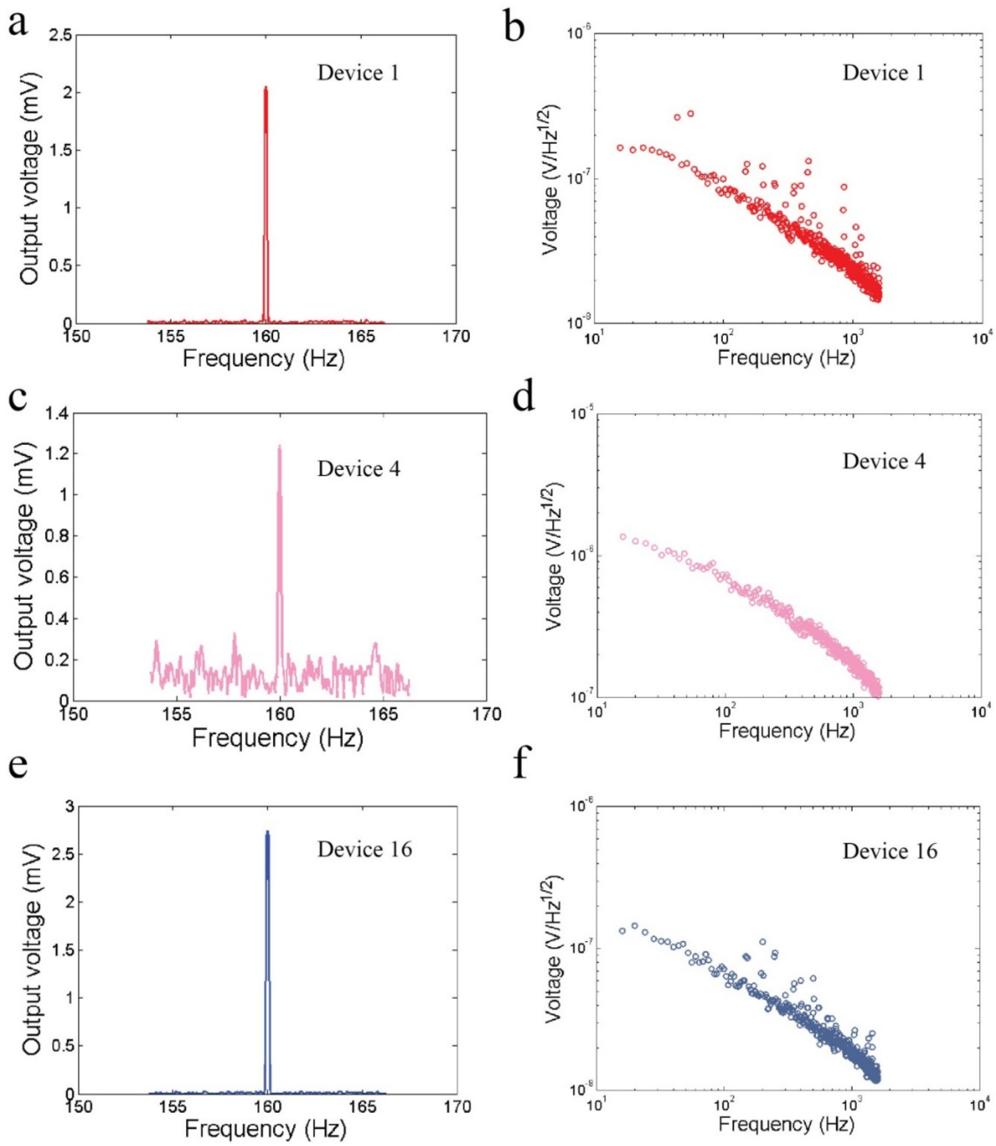

Figure S9| Measured spectrums of output voltages at an applied acceleration of 1 g at a frequency of 160 Hz as measured by the reference accelerometer of the shaker, and noise spectral density (V/ √ Hz) measured without amplification using a spectrum analyser (HP 35670A) in the frequency range from 16 Hz to 1600 Hz (log-log plot). **a** and **b**, device 1. **c** and **d**, device 4. **e** and **f**, device 16.

S11. Control measurements of a device packaged in vacuum

To verify that parasitic effects such as impacts from humidity or gas flow in the vicinity of the graphene transducer are not causing the signal response of our devices, we placed device 5 inside a ceramic package with an actively pumped vacuum of ~10^{-5} bar and exposed it to an acceleration of 1 g at a frequency of 160 Hz as measured by the reference accelerometer. Therefore, the ceramic package containing the wire bonded chip was sealed by soldering a lid on the package (Figure S10b). The lid contains a vacuum connector that is linked via a vacuum pipe to a pressure gauge and a vacuum pump. Measurements of the graphene device were performed while actively pumping a vacuum in the package. These control measurements showed that the output voltages of the device are comparable when it is operated in an actively pumped vacuum of ~10^{-5} bar and when it is operated at atmospheric pressure (1 bar) in air (Figure S11). This demonstrates that the signal response of our devices is not significantly impacted by parasitic effects from humidity or gas flow in the vicinity of the graphene transducer.

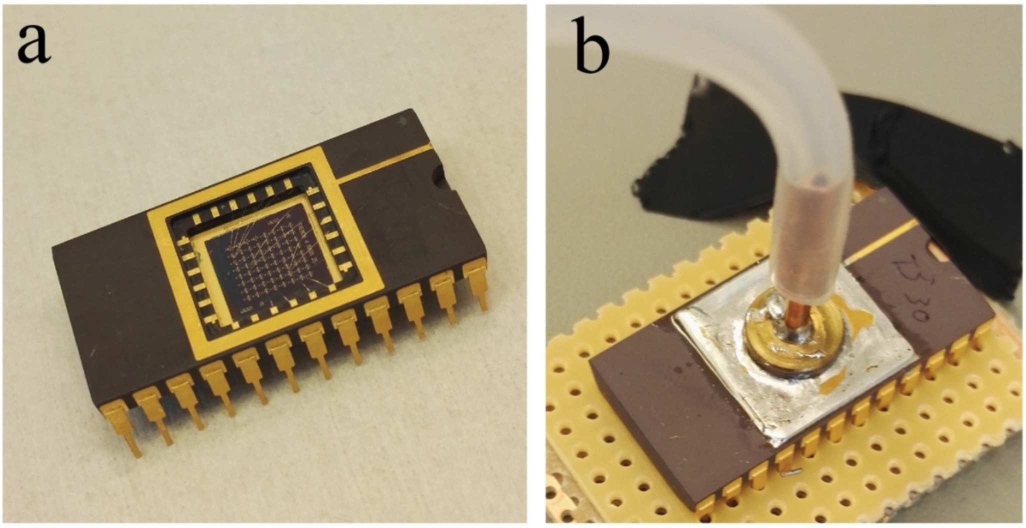

Figure S10| Vacuum packaging of devices. **a,** Photograph of the packaged and wire bonded chip without a lid sealing the ceramic package. **b,** Photograph of the ceramic package that is sealed by a soldered lid containing a vacuum connector that is linked via a vacuum pipe to a pressure gauge and a vacuum pump.

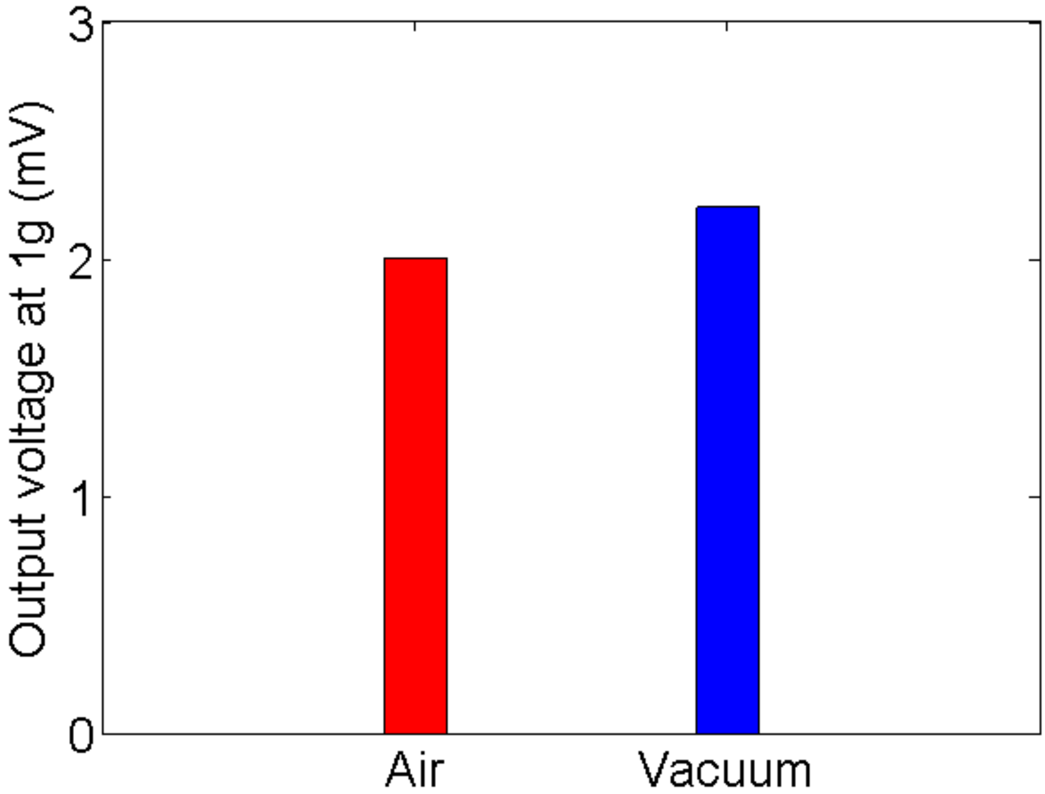

Figure S11| Output voltages of device 5 at an applied acceleration of 1 g at a frequency of 160 Hz as measured by the reference accelerometer of the shaker. The measurement current was 50 μA. The measurements in air were done at a pressure of ~1 bar and in vacuum at a pressure of ~10^{-5} bar.

S12. Measurement repeatability

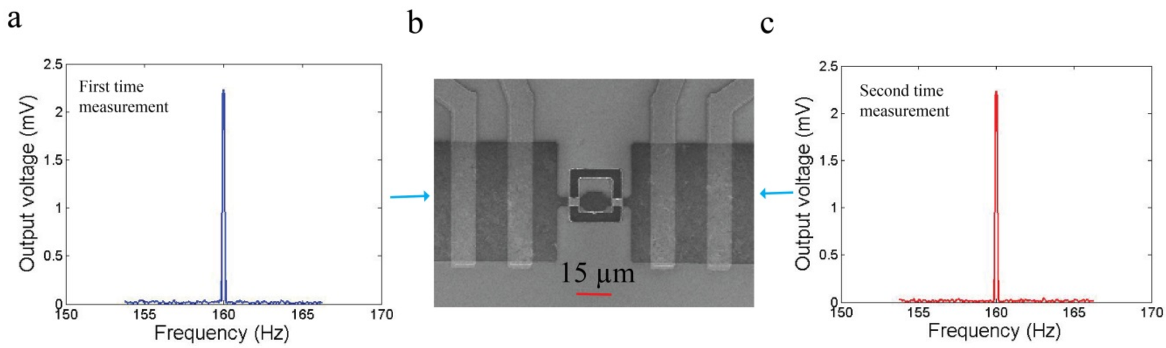

Figure S12| Repeatability of measurements of device 6 when exposed to an acceleration of 1 g at a frequency of 160 Hz as measured by the reference accelerometer of the shaker. **a**, First measurement resulting in an output voltage of 2.229 mV. **b**, SEM image of device 6 in which the proof mass centre is placed with a ~4 µm offset in relation to the centre-line of the graphene ribbon. **c**, Second measurement (about half hour later than the first measurement) resulting in an output voltage of 2.23 mV.

S13. Measurement current versus output voltage of a graphene device

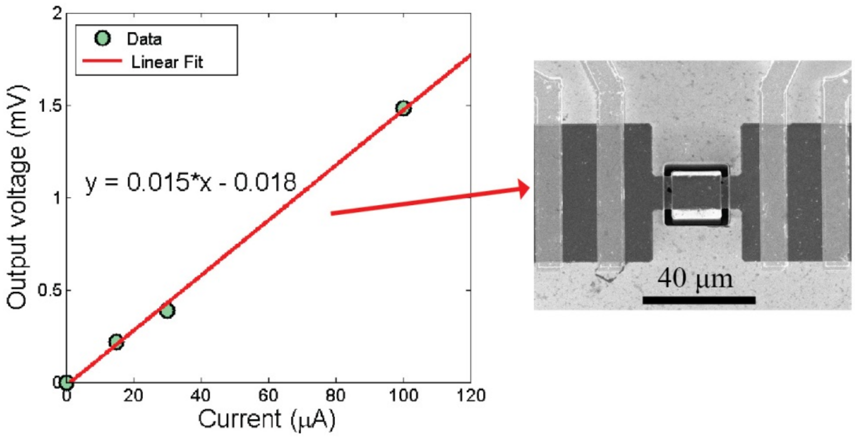

Figure S13| Measurement current versus output voltage of device 7 when exposed to an acceleration of 1 g at a frequency of 160 Hz as measured by the reference accelerometer of the shaker, and SEM image of the device. When using different measurement currents, the output voltage increases proportionally with the measurement current. This confirms consistent and repeatable device functionality.

S14. FEA description of devices and simulation results

The FEA device model in Ansys along with the used elements and parameters are shown in Figure S14. Using this FEA model, the static displacement of the proof mass caused by a force acting on the mass was simulated under different values of built-in stress in the graphene ribbons. The results of these simulations are shown in Supplementary Section S15, Tables S5 and S6. In addition, the resonance frequencies as a function of the built-in stress in the graphene ribbons were investigated. The simulations revealed that the rigid body motion of the proof mass can only take place in a small number of ways as illustrated in Figure S15. In this example the dimensions of device 1 were used in the simulation. The modal analysis illustrates that there are three low-frequency modes that involve rigid body motions of the proof mass (Figure S15a-c). The motion in z-axis direction is the rigid body mode (Z-mode) of the proof mass that is easiest to excite (Figure S15b). A video of the Z-mode movement of the proof mass is available in Supplementary Video 1. Overtones can exist for the rigid body modes, but they have high frequencies, typically several hundred kHz, since they involve unfavorable deformations of the ribbons (Figure S15d-f). In addition, high-frequency eigenmodes with typical frequencies of several hundred kHz can exist that mainly involve deformation and movements of the ribbons (Figure S15d-f). However, these high-frequency membrane modes do not have sufficient energy to move the proof mass.

Using the FEA we studied the frequency response of a device in which the centre of the proof mass is placed with an offset relative to the centre line of the graphene ribbon. An offset of 2 µm, as present in device 4, was evaluated and the simulation results illustrate that the influence of the offset on the low-frequency modes is extremely small (Figure S16). For example, in case of a realistic built-in stress in the ribbons of 250 MPa, the frequency of the Z-mode shifts from 42.28 kHz (without proof mass offset) to 42.9 kHz (with proof mass offset).

a b

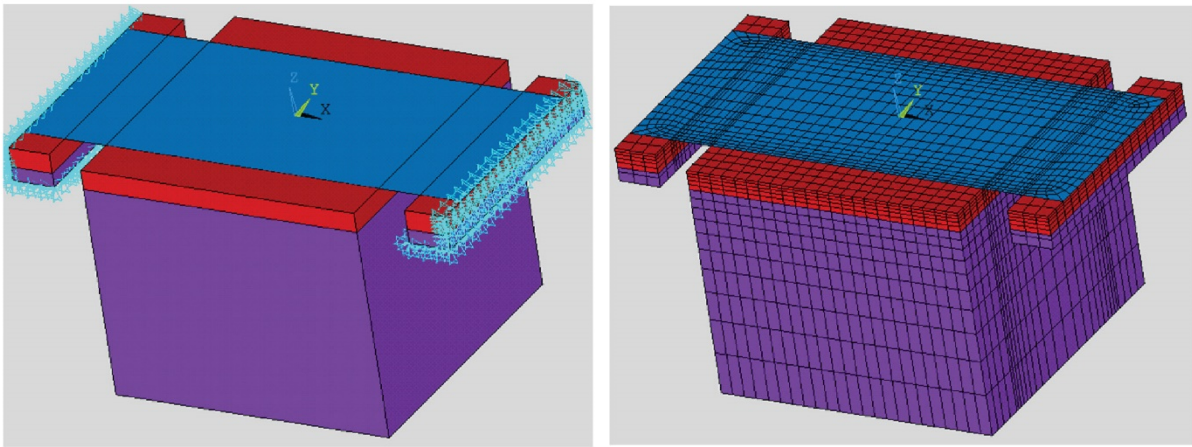

Figure S14| Ansys FEA model. **a**, Three-dimensional model of the complete device structure, including the different materials (graphene, silicon and SiO_2, depicted by blue, red and purple, respectively) and the clamped substrate (fixation depicted by light blue markers). The coordinate system indicates the axes used in the model. **b**, In this model we used ~1 000 shell 4-node elements that account for bending, membrane stress and strain for the graphene, and ~12 000 solid 8-node elements for the proof mass and the anchor regions. Both element types can handle large nonlinear deformations. The proof mass has six degrees of freedom (lateral in directions of the X, Y and Z-axis and rotations around X, Y and Z-axis). We found that the Young's modulus and built-in stresses are the most important material parameters that have significant impacts on the FEA simulation results.

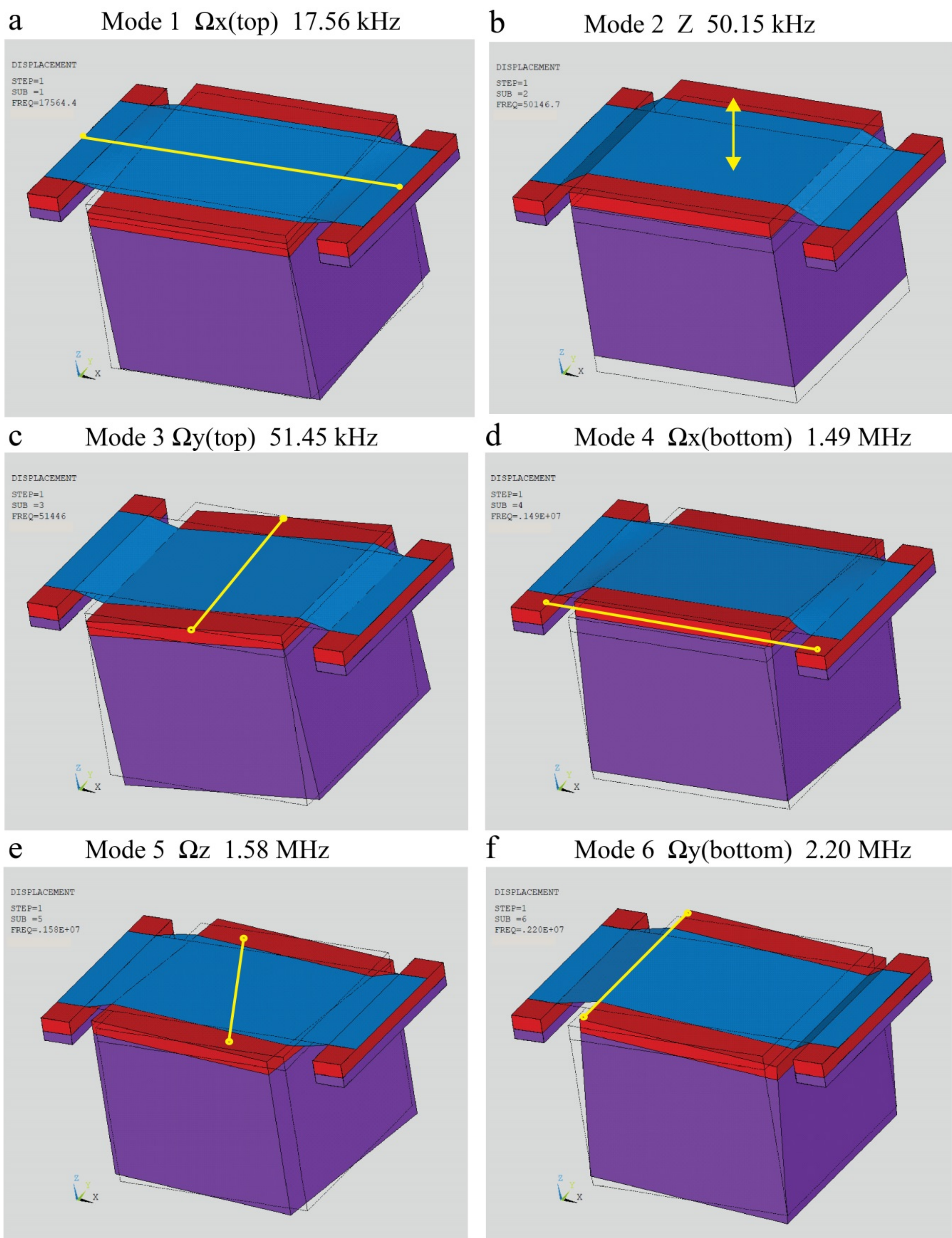

Figure S15| Simulated rigid body modes of a device with dimensions of those of device 1 at a 1 g vibration load, using a Young's modulus of 0.22 TPa and a built-in stress in the graphene ribbons of 250 MPa. **a,** Torsional mode around X-axis (top). **b,** Translational mode along Z-axis. **c,** Torsional mode around Y-axis. **d,** Torsional mode around X-axis (bottom). **e,** Torsional mode around Z-axis. **f,** Torsional mode around Y-axis (bottom).

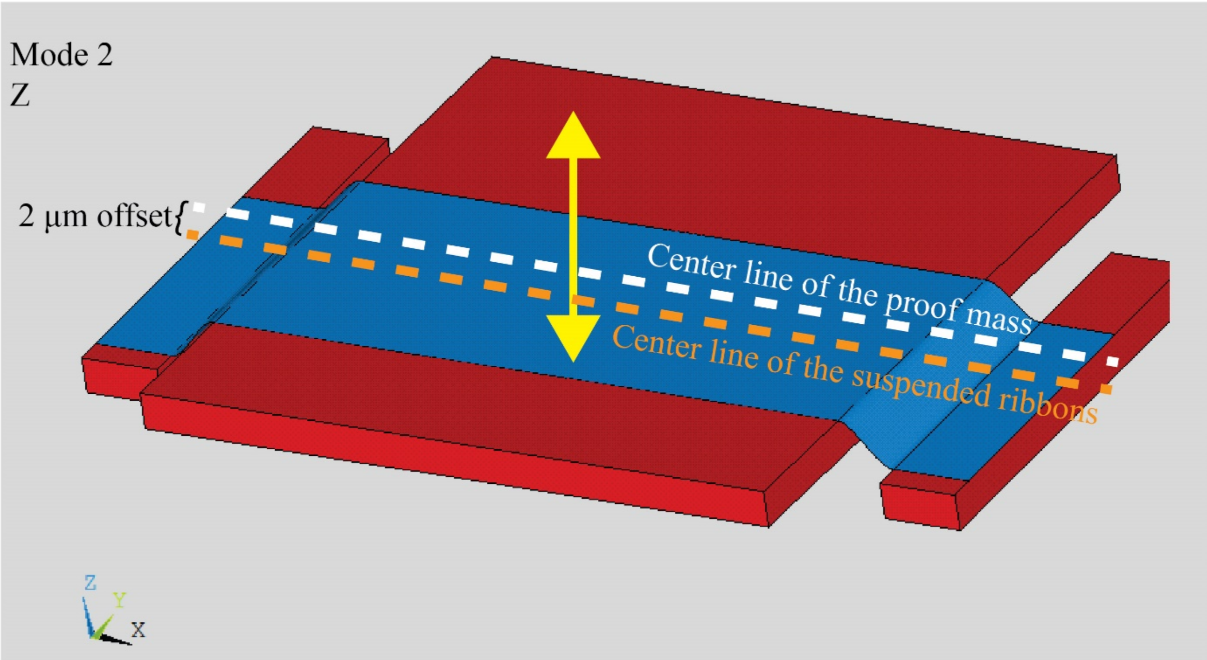

Figure S16| Simulated rigid body Z-mode of device 4 at a 1 g vibration load, using a Young's modulus of 0.22 TPa and a built-in stress in the graphene ribbons of 250 MPa. The centre of the proof mass is placed with a 2 μm offset relative to the centre line of the graphene ribbons. For improved visualization, the image includes only the graphene and SiO_2 layers.

S15. Analytic description of devices

To compare our experimental results with a theoretical description of the devices, we used the system representation shown in Figure S17a as a model for our devices. The two graphene ribbons (regions inside the red dotted lines) deflect in response to a force acting on the proof mass. Since the system is symmetric and the proof mass is rigid compared to the graphene ribbons, the model can be simplified to a single doubly-clamped graphene ribbon with a centre point load (Figure S17b). The effective length L_{SG} of the doubly-clamped single ribbon equals the combined length of the two ribbons, which equals two times the trench width.

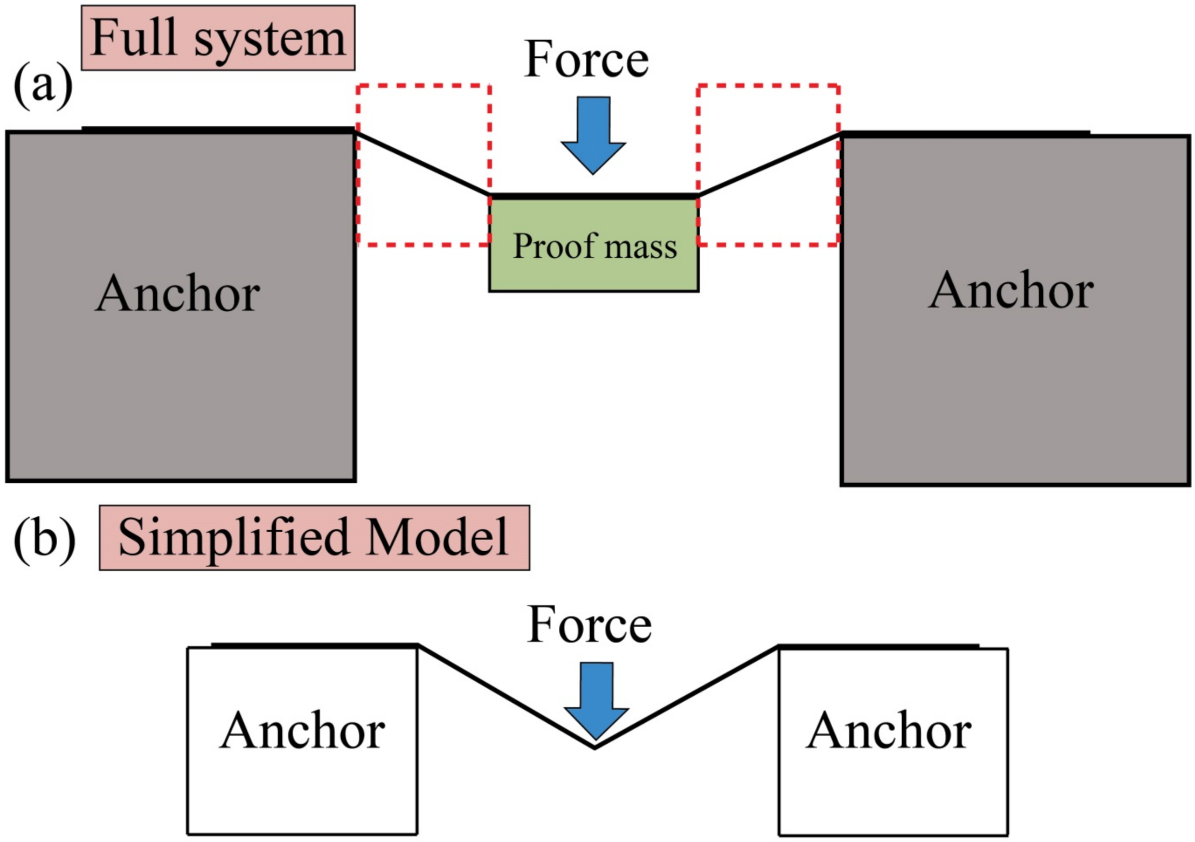

Figure S17| Equivalent model of the devices. **a**, Model of two suspended graphene ribbons with an attached poof mass. The proof mass is displaced in response to a force acting on the mass, thereby deflecting the suspended graphene ribbons. **b**, Simplified device model consisting of a single doubly-clamped graphene ribbon with a centre point load.

For a doubly-clamped ribbon with a centre point load, and large deflections compared to the thickness of the ribbon, the relation between the ribbon-deflection at the centre of the ribbon caused by a centre point load is, according to reference[31], approximated by

$$F = \frac{\pi^4}{8}\left[\frac{EWH}{L^3}\right]Z^3 + \frac{\pi^4}{6}\left[\frac{EWH^3}{L^3}\right]Z + \frac{\pi^2}{2}\left[\frac{T}{L}\right]Z \tag{S1}$$

where F is the load applied at the centre of the ribbon, Z the resulting ribbon deflection at the centre of the ribbon, E the Young's modulus, W the ribbon width, H the ribbon thickness, L the total length of the ribbon, and T the built-in tension force of the ribbon. However, the effect of membrane stress becomes noticeable in multiple-clamped structures when the deflection exceeds half the thickness of the ribbon. For our ribbons the deflection is in most cases well above this limit and the membrane stress will therefore dominate over the bending stress. The deflection shape of the ribbons will reflect this and will be fairly straight between its anchoring points and the proof mass, instead of the conventional smooth sinus-resembling deflection that is characteristic when the bending stress dominates. Thus, the assumption of a sinusoidal ribbon deflection shape is used to derive equation (S1), which is valid for typical beams or ribbons in conventional MEMS structures. However, for typical graphene ribbons a more realistic deflection shape is instead a linear deflection shape. Introducing the linear deflection shape and combining it with the classical handbook expression for small-deflection amplitudes[31], results in an improved equation for the ribbon-deflection at the centre of the graphene ribbon:

$$F = 8\left[\frac{EWH}{L^3}\right]Z^3 + 16\left[\frac{EWH^3}{L^3}\right]Z + 4\left[\frac{T}{L}\right]Z \tag{1}$$

The detailed derivation of the new equation (1) is provided in Supplementary Section S16.

The average residual built-in stress (σ_0) in a doubly-clamped ribbon can be approximated by

$$\sigma_0 = \frac{T}{WH} \tag{S2}$$

A comparison of the calculated ribbon deflection in dependence of different forces using our FEA model and equations (S1) and (1) shows that equation (S1) overestimates the deflection of the graphene ribbon by about 12% for low built-in tension values (if the stress-stiffening Z^3-term dominates the equations), and by about 18% for large built-in tension values (if the tensing-related Z-term dominates the equations). In contrast, the new equation (1) produces more accurate results for all cases (Table S5 and S6). It should be noted that in order to provide an accurate comparison between the FEA model and the analytical equations, the Poisson's ratio of graphene was set to 0 (Table S5 and S6). In addition, we have also performed the simulations using a Poisson's ratio of graphene of 0.25, showing that the Poisson's ratio has no significant effect on the resulting calculated deflections (Table S5 and S6). If the built-in stress in the graphene ribbon is of the order of hundreds of MPa and the applied force is small, the linear terms dominate equation (1) and the nonlinear (cubic) term can be neglected. In this case equation (1) can be simplified to

$$F = 16\left[\frac{EWH^3}{L^3}\right]Z + 4\left[\frac{T}{L}\right]Z \tag{S3}$$

This is a linear system that can be approximated by the standard linear accelerometer model based on a spring-damper-mass system to arrive at the mechanical transfer function[37]

$$\mathrm{H(s)} = \frac{1}{s^2+\frac{D}{M}s+\frac{K}{M}} = \frac{1}{s^2+\frac{2\pi f_0}{Q}s+(2\pi f_0)^2} \tag{2}$$

where D is the damping factor, M is the mass and K is the effective spring constant of the system. The effective spring constant (K) and the damping factor (D) of the system are expressed by

$$\mathrm{K} = (2\pi \mathrm{f}_0)^2\mathrm{m} \tag{S4}$$

$$\mathrm{D} = \frac{\sqrt{\mathrm{Km}}}{\mathrm{Q}} \tag{S5}$$

where m is the mass, Q is the quality factor and f_0 is the resonance frequency. The relationship between the built-in stress and resonance frequency is expressed by

$$\sigma_0 = \frac{L}{4WH}\left[(2\pi f_0)^2 m - \frac{16EWH^3}{L^3}\right] \tag{S6}$$

Using equation (S3) together with geometric considerations, the average strain (ε) in the graphene ribbons, and the gauge factor (GF) of the strain gauge defined by the two suspended graphene ribbons of our devices can be approximated by

$$\varepsilon = \frac{2Z^2}{L^2} = \frac{2(Z_0+z_{acc})^2}{L^2} \approx \frac{F^2}{8\sigma_0^2 W^2 H^2} \tag{S7}$$

$$\mathrm{GF} = \frac{\Delta R_{SG}/R_{SG}}{\varepsilon\ (160\ Hz)} = \frac{\Delta R_{SG}/R_{SG}}{\frac{4Z_0 z_{acc}}{L^2}} \tag{S8}$$ [70]

where Z_0 is the offset deflection resulting from the 1 g acceleration bias from the earth gravitation, and z_{acc} is the displacement resulting from the acceleration.

According to equation (S3), (S7) and (S8), and assuming that the piezoresistive effect is the main contributing factor to the resistance change in the graphene ribbons, the theoretical relationship between the suspended graphene resistance change ΔR_{SG} (equals to ΔR and corresponding to the output voltage) and applied acceleration (a) is

$$\Delta R_{SG} \sim a^2 \tag{S9}$$

If the nonlinear term in equation (1) is sufficiently large so that the linear terms in equation (1) can be ignored, then the average strain (ε) in the graphene ribbons and the theoretical relationship between the suspended graphene resistance change ΔR_{SG} (corresponding to the output voltage) and applied acceleration (a) are

$$\varepsilon = \frac{2Z^2}{L^2} = \frac{2(Z_0+z_{acc})^2}{L^2} \approx \frac{1}{2}\sqrt[3]{\frac{F^2}{E^2W^2H^2}} \tag{S7'}$$

$$\Delta R_{SG} \sim a^{2/3} \tag{S10}$$

TABLE S5. Ribbon deflection of device 9 for different centre-point forces.

Poisson's Ratio	Force (nN)	Centre Point Ribbon Deflection (nm)			Error (%)	
		FEA	Eq. (S1)	Eq. (1)	(FEA- Eq. (S1)) / FEA	(FEA- Eq. (1)) / FEA
0	0.01	7.31	6.55	7.54	10.4%	-3.1%
	0.1	16.1	14.2	16.3	11.8%	-1.2%
	1	35.0	30.5	35.1	12.9%	-0.29%
	10	75.7	65.8	75.7	13.1%	~ 0
	100	163	142	163	12.9%	~ 0
	1000	353	306	351	13.3%	0.6%
0.25	0.01	7.21	6.55	7.54	9.2%	-4.6%
	0.1	15.9	14.2	16.3	10.7%	-2.5%
	1	34.5	30.5	35.1	11.6%	-1.7%
	10	74.7	65.8	75.7	11.91%	-1.3%
	100	161	142	163	11.8%	-1.2%
	1000	349	306	351	12.3%	-0.6%

Footnote: The ribbon deflections of device 9 for different centre-point forces were calculated using the FEA model and equations (S1) and (1), assuming negligible built-in stress (0 MPa) and a Young's modulus of 0.22 TPa.

TABLE S6. Ribbon deflection of device 9 with different built-in stresses.

Poisson's Ratio	Built-in Stress (MPa)	Centre Point Ribbon Deflection (nm)			Error (%)	
		FEA	Eq. (S1)	Eq. (1)	(FEA- Eq. (S1)) / FEA	(FEA- Eq. (1)) / FEA
0	0.01	35	30.5	35.1	12.9%	-0.29%
	0.1	34.8	30.4	35.0	12.6%	-0.57%
	1	33.6	29.3	33.8	12.8%	-0.6%
	10	22.1	18.7	22.3	15.4%	-0.9%
	100	2.97	2.42	2.98	18.5%	-0.3%
	1000	0.291	0.242	0.299	16.8%	-2.8%
0.25	0.01	33.6	30.5	35.1	9.2%	-4.5 %
	0.1	33.5	30.4	35.0	9.3%	-4.5%
	1	32.6	29.3	33.8	10.1%	-3.7%
	10	21.9	18.7	22.3	14.6%	-1.8%
	100	2.97	2.42	2.98	18.5%	-0.3%
	1000	0.291	0.242	0.299	16.8%	-2.8%

Footnote: The ribbon deflections of device 9 with different built-in stresses were calculated using the FEA model and equations (S1) and (1), with a centre point force of 1 nN, and Young's modulus of 0.22 TPa.

S16. Derivation of the analytic equation for the deflection of a centre-loaded doubly clamped graphene ribbon

As shown in chapter 10.4 of Senturia S.D.[31], for large deflections of double-clamped ribbons the stress-stiffening caused by the elongation of the ribbon that causes an in-plane stress in the ribbon has to be accounted for. Similarly, the built-in intrinsic in-plane stress has to be accounted for. An energy method[31] based on virtual work and vibrational methods is a suitable way of addressing this problem. The first step is to calculate the potential energy of the system. The potential energy has three contributions, two of which describe the energy stored in (bending strain energy and stretching strain energy) and one describes the energy added to the system (external work). In Figure S18 a model of the system is shown and the following parameters are defined:

x-axis = along the ribbon

z-axis = perpendicular to the ribbon in the direction of its deformation

δx = the displacement along the ribbon (stretching)

δz = the displacement perpendicular to the ribbon (bending)

$\delta z(x)$ = the displacement's variation over the length of the ribbon

σ_0 = built-in intrinsic stress

ε = strain

E = Young's modulus

L = ribbon's length

W = ribbon's width

w = energy

H = ribbon's thickness

F = the force load applied at the centre of the ribbon

z_o = the resulting ribbon deflection at the centre of the ribbon

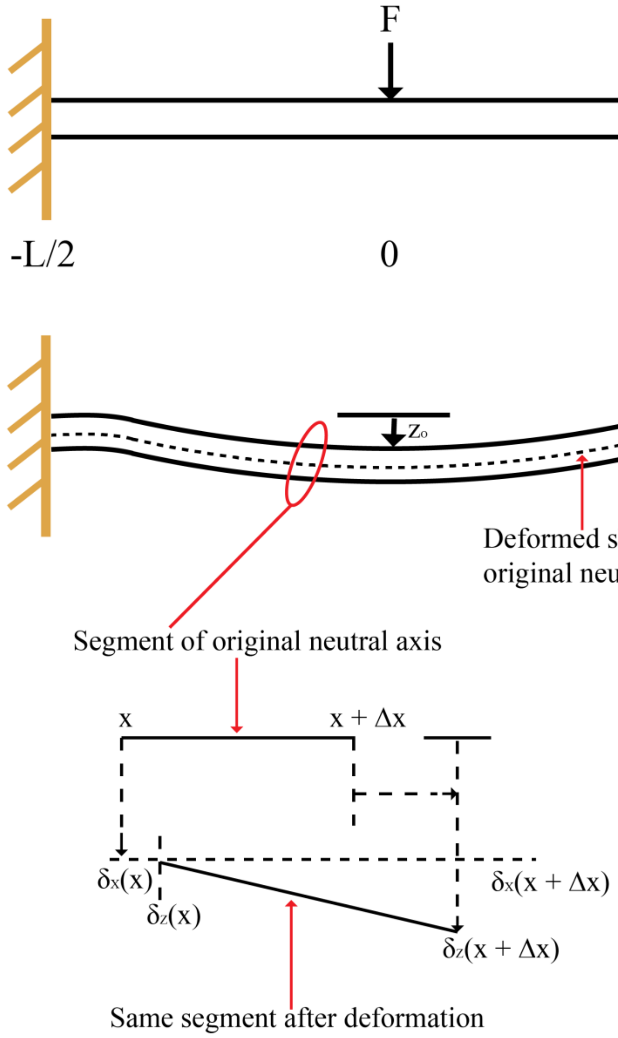

Figure S18| Doubly clamped ribbon with a point load in the centre. The centre deflection Z_O is comparable to, or larger than the ribbon thickness. The expanded view of the segment of the original neutral axis is used to illustrate the components of the deformation in detail (adapted from Figure 10.2 in chapter 10 of Senturia, S.D.[31]).

Determination of the strain due to stretching

1) Strain in segment: the actual length, s, of a thin segment of the ribbon that is located between x and x + Δx and that is stretched for the distance dx in x-direction and deformed for the distance dz in z-direction (see lower part of Figure S18) is given by:

$$s_{segment} = \sqrt{(\Delta x + dx)^2 + dz^2}$$

$$= \sqrt{[\Delta x + (\delta_x(x+\Delta x) - \delta_x(x)]^2 + \left(\delta_z(x+\Delta x) - \delta_z(x)\right)^2}$$

$$= \sqrt{\left[\Delta x + \Delta x \cdot \left(\frac{d\delta_x}{dx}\right)\right]^2 + \left[\Delta x \cdot \left(\frac{d\delta_z}{dx}\right)\right]^2}$$

$$= \Delta x \cdot \sqrt{1 + 2 \cdot \left(\frac{d\delta_x}{dx}\right) + \left(\frac{d\delta_x}{dx}\right)^2 + \left(\frac{d\delta_z}{dx}\right)^2}$$

$$\approx \Delta x \cdot \left[1 + \frac{d\delta_x}{dx} + \frac{1}{2} \cdot \left(\frac{d\delta_z}{dx}\right)^2\right]$$

$$\Delta s_{segment} = s_{segment} - \Delta x = \Delta x \cdot \left[\frac{d\delta_x}{dx} + \frac{1}{2} \cdot \left(\frac{d\delta_z}{dx}\right)^2\right]$$

The local axial strain due to stretching is:

$$\varepsilon_{stretch} = \frac{\Delta s_{segment}}{\Delta x} = \frac{d\delta_x}{dx} + \frac{1}{2} \cdot \left(\frac{d\delta_z}{dx}\right)^2 \qquad \text{(S11)}$$

2) The elongation of the ribbon caused by this stretching results in:

$$\Delta \mathrm{L} = \int_{\frac{-L}{2}}^{\frac{L}{2}} \varepsilon_{stretch}\, dx = \int_{\frac{-L}{2}}^{\frac{L}{2}} \left(\frac{d\delta_x}{dx}\right) dx + \frac{1}{2} \cdot \int_{\frac{-L}{2}}^{\frac{L}{2}} \left(\frac{d\delta_z}{dx}\right)^2 dx$$

The endpoints of the ribbon are clamped and do not move, thus

$$\delta_x\left(\frac{L}{2}\right) - \delta_x\left(\frac{-L}{2}\right) = 0.$$

The first item in this equation is 0 after integration, resulting to

$$\Delta \mathrm{L} = \frac{1}{2} \cdot \int_{\frac{-L}{2}}^{\frac{L}{2}} \left(\frac{d\delta_z}{dx}\right)^2 dx$$

Consequently, the average strain of the ribbon due to stretching is

$$\varepsilon_{stretch.average} = \frac{\Delta L}{L} = \frac{1}{2L} \cdot \int_{\frac{-L}{2}}^{\frac{L}{2}} \left(\frac{d\delta_z}{dx}\right)^2 dx \qquad \text{(S12)}$$

3) The ribbon is homogeneous and thus, the axial stress in the ribbon is constant over the length of the ribbon. A consequence is that also the strain will be constant over the length of the homogenous ribbon, which means that $\frac{d\delta_x}{dx} = 0$, and one can describe the axial strain via its average ($\varepsilon_{stretch.average}$).

4) The situation within the cross-section also has to be accounted for. A curving of the ribbon introduces a local axial strain that varies over the cross-section due to the bending. The standard expression that couples the curving to how the strain varies over the cross-section (assuming z =0 at the centre of the ribbon) is:

$$\varepsilon_{bend} = -z \cdot \frac{d^2\delta_z}{dx^2} \tag{S13}$$

Thus, the resulting expression for the local strain in each point of the cross-section is:

$$\varepsilon_{local} = \varepsilon_{stretch.average} + \varepsilon_{bend} = \frac{1}{2L} \cdot \int_{\frac{-L}{2}}^{\frac{L}{2}} \left(\frac{d\delta_z}{dx}\right)^2 dx - z \cdot \frac{d^2\delta_z}{dx^2} \tag{S14}$$

Compute the stored strain energy in three steps:

1) The strain energy (stretching + bending) stored in a small local volume ΔVol ($\sigma = \sigma_0 + E \cdot \varepsilon$) is:

$$w_{strain.\Delta Vol} = \left[\int_0^{\varepsilon_{local}} (\sigma_0 + E \cdot \varepsilon) d\varepsilon\right] \cdot \Delta Vol = \left(\sigma_0 \cdot \varepsilon_{local} + \frac{E \cdot \varepsilon_{local}{}^2}{2}\right) \cdot \Delta Vol \tag{S15}$$

2) The total energy in the entire volume (sum over all the small volumes) is:

$$w_{strain} = \int \left(\sigma_0 \cdot \varepsilon_{local} + \frac{E \cdot \varepsilon_{local}{}^2}{2}\right) \cdot dVol = \sigma_0 \cdot \int \varepsilon_{local} dVol + \frac{E}{2} \cdot \int \varepsilon_{local}{}^2 \, dVol$$

$$= W \cdot \left(\sigma_0 \cdot \int_{\frac{-L}{2}}^{\frac{L}{2}} \int_{\frac{-H}{2}}^{\frac{H}{2}} \varepsilon_{local} dz \, dx + \frac{E}{2} \cdot \int_{\frac{-L}{2}}^{\frac{L}{2}} \int_{\frac{-H}{2}}^{\frac{H}{2}} \varepsilon_{local}{}^2 dz \, dx\right) \tag{S16}$$

3) Calculate each of these two items of equation (S16) separately by substituting equation (S14) into equation (S16):

$$w_{strain.\sigma} = W \cdot \sigma_0 \cdot \int_{\frac{-L}{2}}^{\frac{L}{2}} \int_{\frac{-H}{2}}^{\frac{H}{2}} \left[\frac{1}{2L} \cdot \int_{\frac{-L}{2}}^{\frac{L}{2}} \left(\frac{d\delta_z}{dx}\right)^2 dx - z \cdot \frac{d^2\delta_z}{dx^2}\right] dz \, dx$$

$$= \sigma_0 \cdot \frac{W \cdot H}{2} \int_{\frac{-L}{2}}^{\frac{L}{2}} \left(\frac{d\delta_z}{dx}\right)^2 dx \tag{S17}$$

$$w_{strain.E} = W \cdot \frac{E}{2} \cdot \int_{\frac{-L}{2}}^{\frac{L}{2}} \int_{\frac{-H}{2}}^{\frac{H}{2}} \left[\frac{1}{2L} \cdot \int_{\frac{-L}{2}}^{\frac{L}{2}} \left(\frac{d\delta_z}{dx} \right)^2 dx - z \cdot \frac{d^2 \delta_z}{dx^2} \right]^2 dz\, dx$$

$$= W \cdot \frac{E}{2} \cdot \left[\int_{\frac{-L}{2}}^{\frac{L}{2}} \int_{\frac{-H}{2}}^{\frac{H}{2}} \left[\frac{1}{4 \cdot L^2} \cdot \left[\int_{\frac{-L}{2}}^{\frac{L}{2}} \left(\frac{d\delta_z}{dx} \right)^2 dx \right]^2 + z^2 \cdot \left(\frac{d^2 \delta_z}{dx^2} \right)^2 \right] dz\, dx \right]$$

$$= W \cdot \frac{E}{2} \cdot \int_{\frac{-L}{2}}^{\frac{L}{2}} \frac{H}{4 \cdot L^2} \cdot \left[\int_{\frac{-L}{2}}^{\frac{L}{2}} \left(\frac{d\delta_z}{dx} \right)^2 dx \right]^2 + \frac{H^3}{12} \cdot \left(\frac{d^2 \delta_z}{dx^2} \right)^2 dx \qquad \text{(S18)}$$

The total stored potential energy is:

$$w_{total.strain} = w_{strain.\sigma} + w_{strain.E} \qquad \text{(S19)}$$

Determine the equilibrium condition

The final aspect that has to be considered is the stored potential energy that should equal the energy supplied by external forces. In the equilibrium, when the force is increased a small amount, the incremental energy supplied must equal the small increase in potential energy. Mathematically it means that:

Δ (supplied energy) = Δ (potential energy), at equilibrium when Δ is small, or written in a different way:

[Δ (potential energy) – Δ (supplied energy)] / Δc = 0,

where c is the amplitude of the deformation and Δ(Fc) = F × Δc is the change in supplied energy. In the following we assume that the external force is a point force and that it is applied at the centre of the ribbon, and that c is the amplitude at this point.

$$w_{potential.total} = w_{potential.stored} - w_{potential.applied} = w_{total.strain} - F \cdot c \qquad \text{(S20)}$$

The equilibrium here is obtained by requiring that:

$$\frac{dw_{potential.total}}{dc} = 0 \qquad \text{(S21)}$$

Apply the general expressions to two specific cases

The above are general expressions. The following are two trial functions for a double-clamped ribbon [-L/2, L/2]:

$$\delta_{Z1}(x) = \frac{z_o}{2} \cdot \left(1 + \cos\left(\frac{2 \cdot \pi \cdot x}{L} \right) \right) \qquad \text{(S22)}$$

$$\delta_{Z2}(x) = z_o \cdot \left(1 - \left| \frac{2 \cdot x}{L} \right| \right) \qquad \text{(S23)}$$

Equation (S22) describes a smooth deflection that is bending-stress dominated, while equation (S23) describes a straight-line shaped deflection that is membrane-stress dominated. In both cases the edges are clamped [δ (± L/2) = 0] and the centre point deflection equals Zo.

In addition, the first trial function (equation (S22)) has also flat ribbons at the clamped ends $\frac{d\delta}{dx}\left(\pm\frac{L}{2}\right) = 0$, while the second trial function (equation (S23)) doesn't. This is in agreement with that the first trial function (equation (S22)) is close to that expected when the bending energy dominates while the second trial function (equation (S23)) is close to that expected when the membrane energy dominates.

$$\frac{d}{dx}\delta_{z1}(x) = \frac{-z_o\cdot\pi}{L}\cdot sin\left(\frac{2\cdot\pi\cdot x}{L}\right) \tag{S24}$$

$$\frac{d}{dx}\delta_{z2}(x) = -\left|\frac{2\cdot z_o}{L}\right| \tag{S25}$$

$$\frac{d^2\delta_{z1}}{dx^2} = \frac{-2\cdot z_o\cdot\pi^2}{L^2}\cdot cos\left(\frac{2\cdot\pi\cdot x}{L}\right) \tag{S26}$$

$$\frac{d^2\delta_{z2}}{dx^2} = 0 \tag{S27}$$

Substituting the above trial functions (equation (S24) - (S27)) into equation (S14) yields:

$$\varepsilon_{local.1} = \left(\frac{z_o\cdot\pi}{2\cdot L}\right)^2 + z\cdot\frac{2\cdot z_o\cdot\pi^2}{L^2}\cdot cos\left(\frac{2\cdot\pi\cdot x}{L}\right) \tag{S28}$$

$$\varepsilon_{local.2} = 2\cdot\left(\frac{z_o}{L}\right)^2 \tag{S29}$$

The indices 1 and 2 denote the results for these two trial functions, combining equation (S17) and (S18) yields:

$$w_{strain.\sigma.1} = \sigma_0\cdot\frac{W\cdot H}{2}\cdot\int_{\frac{-L}{2}}^{\frac{L}{2}}\left(\frac{d\delta_z}{dx}\right)^2 dx = \sigma_0\cdot\frac{W\cdot H}{L}\cdot\left(\frac{z_o\cdot\pi}{2}\right)^2 \tag{S30}$$

$$w_{strain.\sigma.2} = \sigma_0\cdot\frac{W\cdot H}{2}\cdot\int_{\frac{-L}{2}}^{\frac{L}{2}}\left(\frac{d\delta_z}{dx}\right)^2 dx = \sigma_0\cdot\frac{2\cdot W\cdot H}{L}\cdot {z_o}^2 \tag{S31}$$

$$\begin{aligned} w_{strain.E.1} &= W\cdot\frac{E}{2}\cdot\left[\frac{W}{4\cdot L^2}\cdot\left[\left(\frac{z_o\cdot\pi}{L}\right)^2\cdot\frac{L}{2}\right]^2\cdot L + \frac{H^3}{12}\cdot\left(\frac{2\cdot z_o\cdot\pi^2}{L^2}\right)^2\cdot\frac{L}{2}\right] \\ &= W\cdot\frac{E}{2}\cdot\left(\frac{\pi^4\cdot H}{16\cdot L^3}\cdot z_o^4 + \frac{H^3}{6}\cdot\frac{z_o^2\cdot\pi^4}{L^3}\right) \end{aligned} \tag{S32}$$

$$w_{strain.E.2} = W\cdot\frac{E}{2}\cdot\left[\frac{W}{4\cdot L^2}\cdot\left[\frac{(2\cdot z_o)^2}{L}\right]^2\cdot L\right] = \mathrm{E}\cdot\frac{2\cdot W\cdot H}{L^3}\cdot {z_o}^4 \tag{S33}$$

Further substituting the above four equations (S31) - (S34) into equation (S20) yields

$$w_{total.strain.1} = \sigma_0\cdot\frac{W\cdot H}{L}\cdot\left(\frac{z_o\cdot\pi}{2}\right)^2 + E\cdot\frac{\pi^4\cdot W\cdot H}{L^3}\cdot\left(\frac{1}{32}\cdot z_o^4 + \frac{W^2}{12}\cdot z_o^2\right) \tag{S34}$$

$$w_{total.strain.2} = \sigma_0\cdot\frac{2\cdot W\cdot H}{L}\cdot {z_o}^2 + \mathrm{E}\cdot\frac{2\cdot W\cdot H}{L^3}\cdot {z_o}^4 \tag{S35}$$

Substituting equations (S34) and (S35) into equation (S20) yields

$$w_{potential.total.1} = \sigma_0\cdot\frac{W\cdot H}{L}\cdot\left(\frac{z_o\cdot\pi}{2}\right)^2 + E\cdot\frac{\pi^4\cdot W\cdot H}{L^3}\cdot\left(\frac{1}{32}\cdot z_o^4 + \frac{W^2}{12}\cdot z_o^2\right) - F\cdot z_o \tag{S36}$$

$$w_{potential.total.2} = \sigma_0 \cdot \frac{2 \cdot W \cdot H}{L} \cdot {z_o}^2 + \mathrm{E} \cdot \frac{2 \cdot W \cdot H}{L^3} \cdot {z_o}^4 - F \cdot z_o \tag{S37}$$

Taking the derivative $\frac{dw_{potential.total}}{dc} = 0$ yields the fundamental expressions that describe the equilibrium:

$$F_1 = \frac{\pi^2}{2} \cdot \frac{W \cdot H}{L} \cdot \sigma_0 \cdot z_o + \frac{\pi^4}{8} \cdot \frac{W \cdot H}{L^3} \cdot E \cdot z_o^3 + \frac{\pi^4}{6} \cdot \frac{W \cdot H^3}{L^3} \cdot E \cdot z_o \tag{S38}$$

$$F_2 = 4 \cdot \frac{W \cdot H}{L} \cdot \sigma_0 \cdot z_o + 8 \cdot \frac{W \cdot H}{L^3} \cdot E \cdot z_o^3 \tag{S39}$$

Equation (S39) gives a poor result (negligible deflection) for very small deflections and no intrinsic stress since its deflection shape does not account for the bending energy. This can easily be addressed by adding the classical handbook response for a double-clamped ribbon[31]. This term will only affect the result in the regime where the expression fails since it has a negligible influence when the deflection or the intrinsic stress gets larger. The expression for F_2 (equation (S39)) then becomes

$$F_2 = 4 \cdot \frac{W \cdot H}{L} \cdot \sigma_0 \cdot z_o + 8 \cdot \frac{W \cdot H}{L^3} \cdot E \cdot z_o^3 + 16 \cdot \frac{W \cdot H^3}{L^3} \cdot E \cdot z_o \tag{S40}$$

which is identical to equation (1):

$$F = 8 \left[\frac{EWH}{L^3}\right] Z^3 + 16 \left[\frac{EWH^3}{L^3}\right] Z + 4 \left[\frac{T}{L}\right] Z \tag{1}$$

Expression for nonlinear spring behaviour

Taking the derivative of F with respect to the amplitude at the deflection (c), we get an expression for the nonlinear spring constant for the ribbon:

$$k_1 = \frac{\pi^2}{2} \cdot \frac{W \cdot H}{L} \cdot \sigma_0 + \frac{3 \cdot \pi^4}{8} \cdot \frac{W \cdot H}{L^3} \cdot E \cdot z_o^2 + \frac{\pi^4}{6} \cdot \frac{W \cdot H^3}{L^3} \cdot E \tag{S41}$$

$$k_2 = 4 \cdot \frac{W \cdot H}{L} \cdot \sigma_0 + 24 \cdot \frac{W \cdot H}{L^3} \cdot E \cdot z_o^2 + 16 \cdot \frac{W \cdot H^3}{L^3} \cdot E \tag{S42}$$

The resonance frequency for a spring-mass system with the mass located at the point where the force is applied is given by:

$$f_0 = \frac{1}{2 \cdot \pi} \cdot \sqrt{\frac{k_o}{mass}} \tag{S43}$$

This expression is valid also for a nonlinear system when the vibration amplitude is sufficiently small that the k value is the same over the entire vibration cycle. In this case $k_o = k_1$ or k_2, where z_o is the "DC" offset of the vibration's deflection around which the vibration takes place. In case the vibration is so large that the spring constant varies over the vibration cycle this expression for the resonance frequency cannot be applied.

S17. Force-displacement measurements using AFM indentation

Force versus proof mass displacement of devices 8 to 11 was measured using indentation with the AFM (Dimension Icon, Bruker) tip at the centre of the suspended proof masses. As shown in Fig. 3b, the resulting force-displacement curves of devices 8 and 9, respectively. The suspended double-layer graphene ribbons survived the largest used indentation force of 1000 nN, resulting in proof mass displacements of 374 nm and 310 nm in devices 8 and 9, respectively. We did not observe any failure of any double-layer graphene ribbon in the AFM indentation measurements, confirming the robustness of the structures. As shown in Fig. 3b, force-displacement data points of the proof masses of devices 10 and 11 using AFM indentation with force up to 200 nN. Table S7 shows the force-displacement measurements using indentation with the AFM tip at positions on the proof masses that have different offsets in relation to the centre line of the graphene ribbons and corresponding calculations by equation (1) and FEA simulations based on a Young's modulus of 0.22 TPa and a built-in stress of 318 MPa. When the force is close to the centre of the proof mass, there is good agreement between the measurement results and the FEA for these experiments. When the placement of the indentation force has an offset, although there are non-ignorable differences of deflection values at the same applied force between AFM experiments and FEA simulations, there is an agreement in the trend that the deflection is significantly increased with applied force between AFM experiments and FEA simulations. It should be noted that the accurate offset values of the AFM tip acting on the proof mass are not exactly known and are probably not exactly equal to the 4 μm and 8 μm offset that we use in the FEA simulations. In addition, the accuracy of the simulations is harder to estimate when a large indentation force is placed with an offset and the deflection becomes larger since there are no simple nonlinear analytical predictions to compare with. The rotational deflections of the ribbons that are created by the large AFM indentation forces appear to complicate the mechanical behaviour.

TABLE S7. Comparison of AFM force displacement of device 8 between centre indentation and off-centre indentation.

AFM indentation measurements			Theoretical calculations and simulations		Equation (1)	FEA simulation
	Force (nN)	Deflection (nm)		Force (nN)	Deflection (nm)	Deflection (nm)
AFM tip close to the centre of the proof mass	10	20	A single point force acting on the centre of proof mass	10	15.6	16
	100	118		100	119.5	119
	1000	374		1000	379.8	379
AFM tip off-centre of the proof mass to some extent (~4 µm)	10	61	A single point force acting on the proof mass with 4 µm offset from the centre	10	-	95
	100	241		100	-	427
	1000	1400		1000	-	1061
AFM tip close to the edge of the proof mass	10	115	A single point force acting on the proof mass with 8 µm offset from the centre	10	-	304
	100	385		100	-	1107

Footnote: Corresponding calculations by equation (1) and FEA simulations were based on a Young's modulus of 0.22 TPa and a built-in stress of 318 MPa.

TABLE S8. Comparison of the strain in suspended graphene caused by AFM indentation experiments.

Author	Type	Thickness (nm)	Force (nN)	Deflection (Z) (nm)	Length (L) (µm)	Radius (a) (µm)	Strain (excl. built-in strain) (ε)*
This work	Doubly-clamped ribbons	Double-layer	1000	374	8		$\sim 4.4 \times 10^{-3}$
Gómez-Navarro[9]	Doubly-clamped ribbons	Single-layer	~17.5	~24	~0.65		$\sim 2.75 \times 10^{-3}$
Shivaraman[29]	Doubly-clamped ribbons	Single-layer	~18	~33	~11		$\sim 1.8 \times 10^{-5}$
Frank[30]	Doubly-clamped ribbons	Graphene sheets (2-8 nm)	~18	~12	~1.2		$\sim 2 \times 10^{-4}$
Traversi[33]	Doubly-clamped ribbons	Single-layer graphene	~17	~15	~1		$\sim 4.5 \times 10^{-4}$
Li[34]	Doubly-clamped ribbons	Graphene sheets (1-5 nm)	~60	~90	~4.2		$\sim 9.2 \times 10^{-4}$
Huang[42] **	Doubly-clamped ribbons	Single-layer	~1800	~100	~ 1		$\sim 2.6 \times 10^{-2}$
Lee[6]	Fully-clamped circular membranes	Single-layer graphene	~1200	~120		~0.75	$\sim 1.7 \times 10^{-2}$
Guillermo[14]	Fully-clamped circular membranes	Single-layer graphene	~550	~80		~0.5	$\sim 1.7 \times 10^{-2}$
Lee[50]	Fully-clamped circular membranes	Single-layer graphene	~2000	~95		~0.75	$\sim 1.07 \times 10^{-2}$
Annamalai[71]	Fully-clamped circular membranes	Single-layer graphene	~560	~128		~1.88	$\sim 3.1 \times 10^{-3}$
Poot[72]	Fully-clamped circular membranes	Graphene flakes (~69 layers)	unknown	~15		~0.5	$\sim 6 \times 10^{-4}$
Bunch[36]	Fully-clamped square membranes***	Single-layer	~10.7	~30		~2.375	$\sim 1.06 \times 10^{-4}$

* Strain for a doubly-clamped ribbon is estimated to $\varepsilon = 2Z^2/L^2$ while strain for a fully-clamped circular membrane is estimated to $\varepsilon = 2Z^2/3a^2$, where Z is the deflection of the suspended graphene, L is the length of a doubly-clamped suspended graphene ribbon, a is the radius of a fully-clamped suspended circular or square graphene membrane.

** This work used a specially designed wedge indentation tip inside a custom indentation instrument composed of a field-emission gun in a vacuum chamber to apply loads on short ribbons made of exfoliated graphene flakes. Thus, this work does not involve AFM indentation.

*** Fully clamped square membranes are approximately assumed to be fully clamped inscribed circular membranes.

S18. Device failure mode

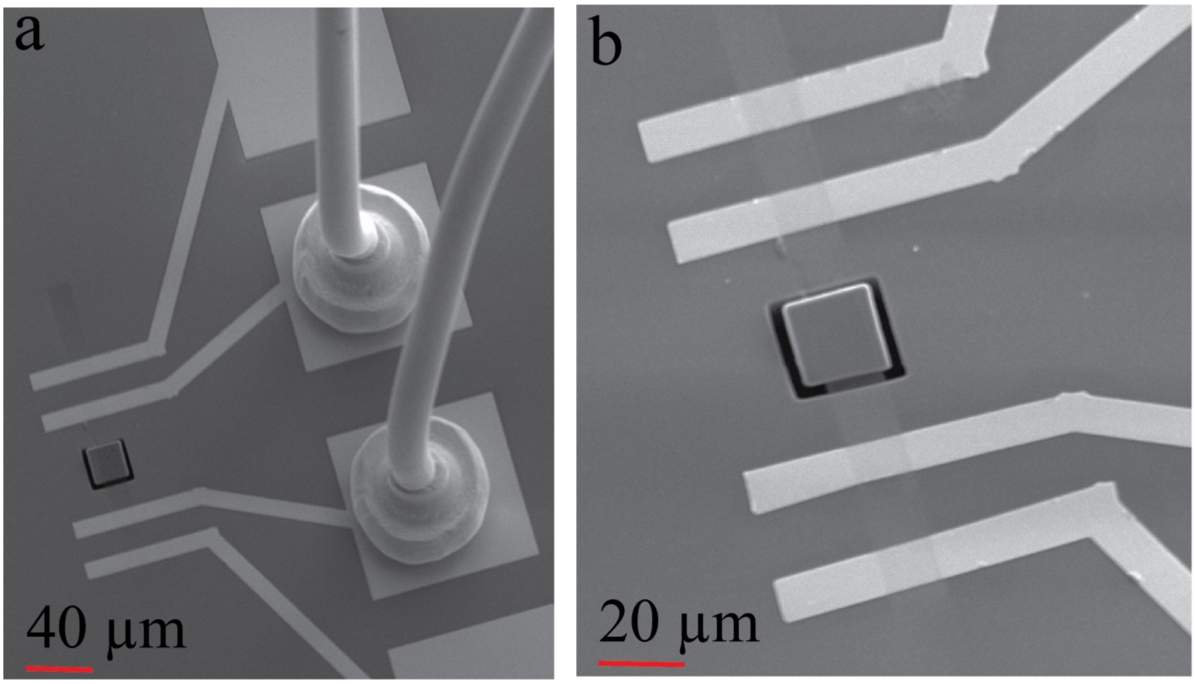

Figure S19| Illustration of the typical failure mode of graphene devices after exposure to excessive shocks during device handling. **a**, SEM image of a defected device with proof mass dimensions of 40 µm × 40 µm × 16.4 µm, ribbon width of 12 µm, and length of the two graphene ribbons of 2 × 3 µm. The proof mass is tilted and sticking to a trench sidewall. **b**, SEM image with close-up of the device in **a**.

S19. Laser Doppler vibrometry (LDV) measurements

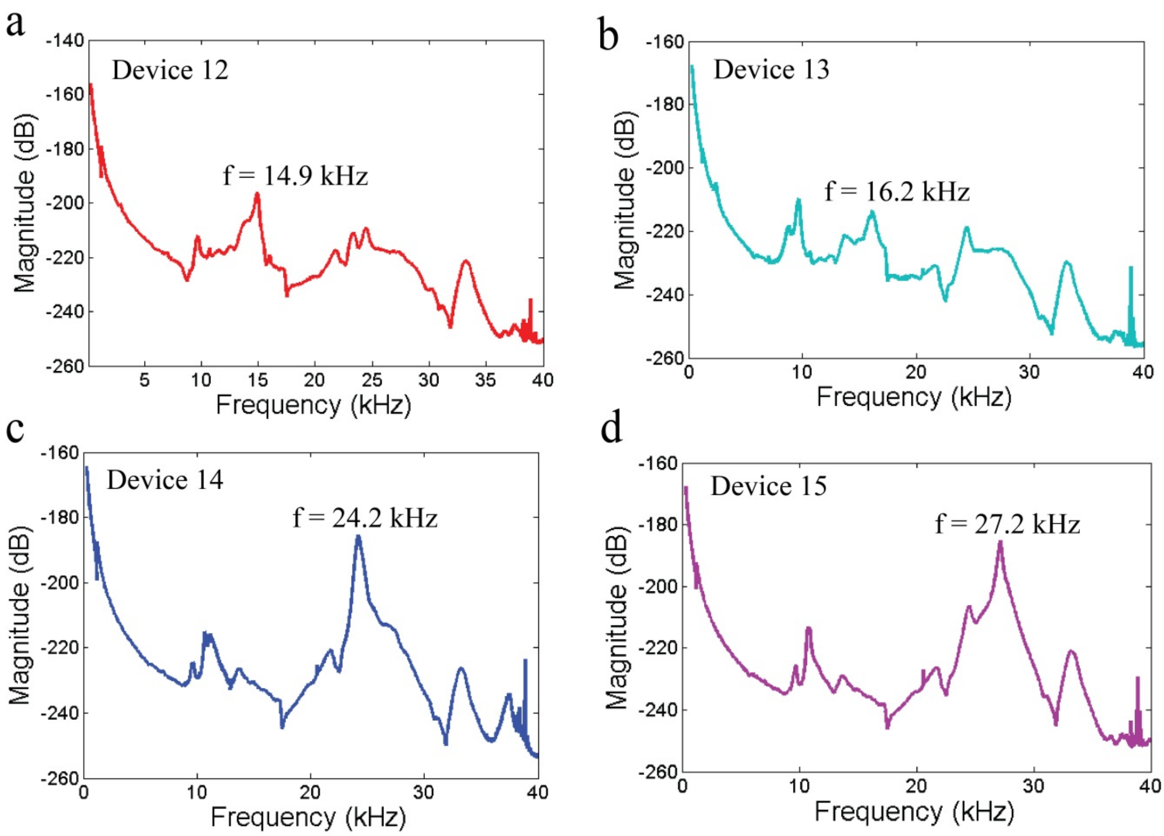

Figure S20| LDV frequency scans of device 12 (**a**)**,** device 13 (**b**) device 14 (**c**) and device 15 (**d**) measured by LDV using a piezo-voltage of 0.1 V for the shaker to actuate the devices. The extracted resonance frequencies of devices 12, 13, 14 and 15 are 14.9 kHz, 16.2 kHz, 24.2 kHz, and 27.2 kHz respectively. The acceleration values at the shaker measured by the reference accelerometer are of the order of 0.0022 g, 0.0018 g, 0.0082 g, and 0.0032 g at frequencies of 14.9 kHz, 16.2 kHz, 24.2 kHz, and 27.2 kHz respectively, which are resolved in the frequency domain using fast Fourier transform (FFT). The features of the peaks in the frequency spectra of devices 12 to 15 (in **a**, **b, c** and **d**) are detailed in Tables S9, S10, S11 and S12 respectively. Most of the frequency peaks are believed to be spurious modes caused by parts external to the proof mass and the graphene ribbon. If we use the resonance frequencies 14.9 kHz (device 12), 16.2 kHz (device 13), 24.2 kHz (device 14), and 27.2 kHz (device 15) to provide an approximate estimate of the quality factors (Q), they are on the order of 62.5, 42.3, 77.5 and 112.7 for devices 12, 13, 14 and 15 respectively.

TABLE S9. Peaks in the measured frequency spectrum of device 12.

Device 12: Frequency scan from 300 Hz to 40 kHz at 0.1 V piezo-voltage of shaker			
Frequency peak (kHz)	Type	Movement of frame	Vibration mode
1.225	Spurious	Substantial	Z dominant
9.713	Spurious	Small	Z dominant
10.65	Spurious	Large	Ω_x dominant
14.9	True resonance	Near static	Z
16	Spurious	Very small (in-plane movement)	Combination of Z, Ω_x and Ω_y
21.813	Spurious	Medium	Ω_y
23.338	Spurious	Medium	Slight Ω_y
24.5	Spurious	Large	Slight Ω_y
33.188	Spurious	Substantial	Z

TABLE S10. Peaks in the measured frequency spectrum of device 13.

Device 13: Frequency scan from 300 Hz to 40 kHz at 0.1 V piezo-voltage of shaker			
Frequency peak (kHz)	Type	Movement of frame	Vibration mode
1.225	Spurious	Substantial	Z dominant
8.737	Spurious	Small (in-plane movement)	Ω_y dominant
9.675	Spurious	Small (in-plane movement)	Ω_y dominant
10.7	Spurious	Medium	Combination of Z, Ωx and Ωy
11.61	Spurious	Medium	Z dominant
12.51	Spurious	Medium	Combination of Z and Ω_y
13.7	Spurious	Small	Ω_y
14.87	Spurious	Small	Ω_y
15.91	Close to true resonance	Near static	Z
16.17	True resonance	Near static	Z
22.88	Spurious	Large	Z
24.5	Spurious	Large	Z
31	Spurious	Large	Z
33.26	Spurious	Substantial	Z

TABLE S11. Peaks in the measured frequency spectrum of device 14.

Device 14: Frequency scan from 300 Hz to 40 kHz at 0.1 V piezo-voltage of shaker			
Frequency peak (kHz)	Type	Movement of frame	Vibration mode
1.225	Spurious	Substantial	Z
9.675	Spurious	Very small	Ω_x dominant
10.7	Spurious	Very small (in-plane movement)	Ω_x
11.15	Spurious	Very small (in-plane movement)	Ω_x
13.713	Spurious	Small	Ω_x dominant
21.775	Spurious	Medium	Z dominant
24.213	True resonance	Near Static	Z
33.212	Spurious	Large	Ω_y dominant
37.5	Spurious	Near static	Ω_y

TABLE S12. Peaks in the measured frequency spectrum of device 15.

Device 15: Frequency scan from 300 Hz to 40 kHz at 0.1 V piezo-voltage of shaker			
Frequency peak (kHz)	Type	Movement of frame	Vibration mode
1.225	Spurious	Substantial	Z
9.68	Spurious	Very small (in-plane movement)	Ω_x dominant
10.7	Spurious	Small (in-plane movement)	Ωx
13.71	Spurious	Small	Ω_x dominant
17.26	Spurious	Small	Combination of Z, Ω_x and Ω_y
21.77	Spurious	Medium	Z dominant
24.49	Spurious	Small to medium	Z
27.2	True resonance	Near static	Z
31.07	Spurious	Medium	Z
33.22	Spurious	Medium	Z

From the LDV measured proof mass displacements listed in Table S13 it can be seen that for device 12 the averaged measured displacements for applied accelerations of 0.5 g and 1g at a frequency of 160 Hz are about 11 ± 2 nm and 22 ± 3 nm, respectively. These proof mass displacements are much higher than those of about 0.75 ± 0.25 nm and 1.25 ± 0.25 nm, respectively, for the same applied accelerations of 0.5 g and 1 g at a frequency of 9.725 kHz, at which the peak in the frequency scan is assumed to be an artefact and mostly likely from the measurement platform rather than from graphene devices. This is because the peak at around 9.725 kHz was always observed in the commercial reference accelerometer during each frequency scan. In device 13 the averaged measured displacement at applied accelerations of 0.5 g and 1g at a frequency of 160 Hz are about 17 ± 2 nm and 31 ± 4 nm, respectively, which are also higher than those of device 12 at the same measurement conditions. The substantial differences in proof mass deflection at different actuation frequencies in our devices is a strong indication that resonances of system parts that are external to the proof mass and the graphene ribbons distort the real effective acceleration acting on the proof mass of the devices. This can cause significant amplifications of the acceleration acting on the proof mass, resulting in actual accelerations that are more than one order of magnitude higher than the acceleration introduced by the shaker. This in turn would lead to proof mass displacements that are much larger than expected. It should be noted that there are significant uncertainties in the LDV measurements of very small proof mass deflections, including due to possible frequency effects.

TABLE S13. LDV proof mass displacement measurements of devices 12 and 13 at applied accelerations (0.5 g and 1 g) at fixed frequencies as measured by the reference accelerometer.

Device 12				
Applied acceleration at fixed frequency	0.5 g at 160 Hz	1 g at 160 Hz	0.5 g at 9.725 kHz	1 g at 9.725 kHz
Measured average displacement (nm)	~ 11 ± 2	~ 22 ± 3	~ 0.75 ± 0.25	~ 1.25 ± 0.25
Device 13				
Applied acceleration at fixed frequency	0.5 g at 160 Hz	1 g at 160 Hz		1 g at 16 kHz
Measured average displacement (nm)	~ 17 ± 2	~ 31 ± 4		~ 10 ±1
Device 14				
Applied acceleration at fixed frequency	0.5 g at 20 kHz	1 g at 20 kHz	0.5 g at 21.688 kHz	1 g at 21.688 kHz
Measured average displacement (nm)	~ 1.5 ± 0.5	~ 3 ± 0.5	~ 6 ± 1	~ 12 ± 2

S20. Comparison of built-in stress and tension of suspended graphene structures

TABLE S14. Comparison of the built-in stress and tension of clamped graphene devices.

Author	Year	Graphene type	Structure	Thickness (nm)	Measurement method	Built-in stress (MPa)	Built-in tension
Present work	2019	CVD	Doubly-clamped suspended graphene ribbons with attached proof mass	Double-layer (~0.67 nm)	Mechanical resonance frequency	$\sim 2 \times 10^2$	$\sim 10^{-6}$ N
					AFM indentation	$\sim 3 \times 10^2$	
Davidovikj[73]	2017	Mechanical exfoliation	Fully-clamped suspended membrane on circular cavity	Multi-layer graphene flake (5 nm)	Electrostatic resonance	$\sim 2\times 10^1$	0.107 N/m
					AFM indentation	$\sim 2\times 10^1$	0.093 N/m
Patel[74]	2016	Mechanical exfoliation	Graphene drum	Multi-layer graphene flake (~ 7.5 nm)	Mechanical resonance	$\sim 3 \times 10^2$	
Lopez-Polin[14]	2015	Mechanical exfoliation	Graphene drum	Single-layer (~0.335 nm)	AFM indentation	$\sim 1.5 \times 10^2$- $\sim 2.4 \times 10^3$	0.05-0.8 N/m
Lee[75]	2013	CVD	SU-8 polymer-clamped graphene drum	Single-layer (~0.335 nm)	Mechanical resonance	$\sim 2.3 \times 10^3$	
Annamalai[71]	2012	Mechanical exfoliation	Fully-clamped suspended membrane on circular cavity	Single-layer to five layer (0.335 to 1.675 nm)	AFM indentation	$\sim 10^3$	0.79-2.3 N/m
Ruiz-Vargas[23]	2011	CVD	Fully-clamped suspended membrane on circular cavity	Single-layer (~0.335 nm)	AFM indentation	$\sim 2.5 \times 10^2$ (average value)	0.085 N/m (average value)
Zande[76]	2010	CVD	Doubly-clamped suspended beam over trench	Single-layer (~0.335 nm)	Mechanical resonance	$\sim 10^1$	
Chen[77]	2009	Mechanical exfoliation	Doubly-clamped suspended beam over trench	Single-layer (~0.335 nm)	Mechanical resonance	$\sim 10^1$ - 10^2	
Bunch[36]	2008	Mechanical exfoliation	Fully-clamped suspended membrane on well	Single-layer (~0.335 nm)	Pressurized blister tester and resonance frequency	$\sim 2 \times 10^2$	~0.06 N/m
					Theoretical estimation by van der Waals interaction	$\sim 3 \times 10^2$	~0.1 N/m

Lee[6]	2008	Mechanical exfoliation	Fully-clamped suspended membrane on circular cavity	Single-layer (~0.335 nm)	AFM indentation	~2.1×10^{2}- ~2.2×10^{3}	0.07 - 0.74 N/m
Poot[72]	2008	Mechanical exfoliation by adhesive tape	Fully-clamped suspended membrane on circular cavity	Graphene flakes (< 33 nm)	AFM indentation	~10^{2}	~0.2 – 15 N/m
Gómez-Navarro[9]	2008	Chemical reduction of graphene oxide	Doubly-clamped suspended beam over trench	Single-layer (~0.335 nm)	AFM indentation	~10^{1}	~4×10^{-9} N
Garcia-Sanchez[37]	2008	Mechanical exfoliation	Doubly-clamped suspended beam over trench	Multi-layer graphene sheets	Electrostatical resonance	~1.5×10^{3}	
Bunch[10]	2007	Mechanical exfoliation	Doubly-clamped suspended graphene over trench	Single-layer (~0.335 nm)	Electrical or optical resonance	~ 2.2×10^{1}	1.3×10^{-8} N
				Graphene sheets (< 7 nm)	Electrical or optical resonance	~10^{-1} - 10^{1}	10^{-8} - 10^{-6} N
Frank[30]	2007	Mechanical exfoliation	Doubly-clamped suspended graphene over trench	Graphene sheets (2-8 nm)	AFM indentation	~10^{1}	3×10^{-7} N

S21. Geometric considerations at the graphene anchors

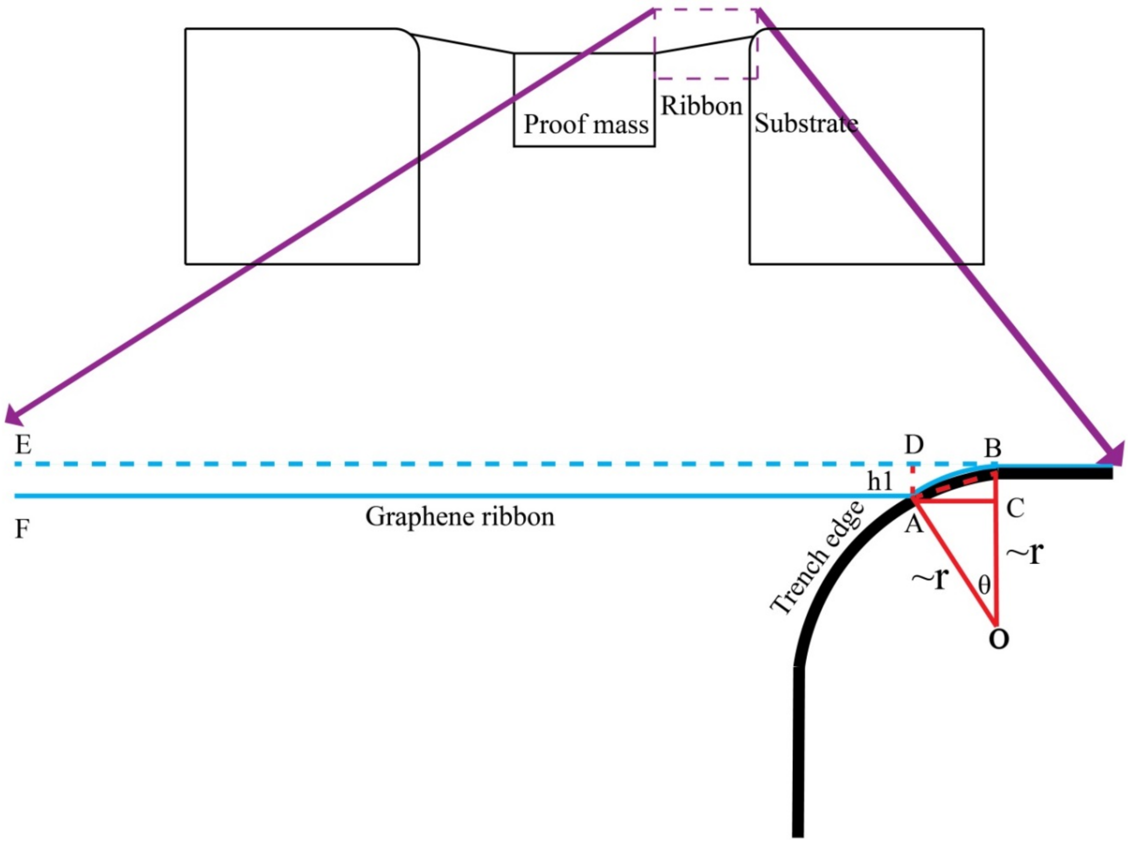

Figure S21| Schematic of the geometric situation at the trench edge, i.e. the anchor points of the graphene ribbons.

Figure S21 illustrates the geometric situation at the anchor points of the graphene ribbons. The van der Waals interactions between the graphene and the SiO_2 surface are comparably strong, causing "roll-down" of the graphene along the rounded edges of the substrate at the trenches and thereby tensioning of the graphene ribbon. The roll-down caused by the van der Waals forces is counteracted by the tensioning/straining of the graphene ribbon, resulting in an equilibrium situation between the "roll-down" and the build-in stress of the graphene ribbon. This means that there will be a “competition” between the adhesion forces wanting to increase the adhesion area, and the tension force in the graphene ribbon that wants to delaminate the graphene from the SiO_2 surface. We expect that a part of the build-in stress is generated in the suspended graphene ribbon in this way, mainly determined by the geometry at the graphene anchor points and by the strength of the van der Waals interactions. It should be noted that the same effect may exist at both anchor points, i.e. also at the attachment point between the proof mass and the graphene ribbons.

To evaluate the plausibility of this hypothesis, we use $\varepsilon = \frac{\sigma_0}{E}$ to arrive at an estimated strain of 0.114% in a 3 μm long suspended graphene ribbon, assuming a graphene Young's modulus of 0.22 TPa and built-in stress in the graphene ribbon of 250 MPa. The corresponding elongation of the 3 μm long ribbon is estimated to be of the order of 3.4 nm, according to $\Delta L = \varepsilon L$. Assuming a radius of about 100 nm of the surface at the anchors edge along which the graphene is pulled towards the SiO_2 surface, a ribbon elongation of the order of 1.5-8.1 nm would be realized if the roll-down causes a vertical ribbon displacement h_1 (Figure S21) in the order of 10-30 nm (corresponding to the angle θ of 26-46°). The exact displacement depends on the exact radius of the anchor edges, the strength of the van der Waals interactions and the pre-stain (or possible pre-existing folds) in the graphene ribbon. This analysis is consistent with our measurements of the static displacement of the released proof masses in our devices, which is in a range between 20-300 nm (Supplementary Section S3). The large static deflections on some of our devices indicates that pre-existing folds have been present in the graphene ribbons prior to the release of the proof mass, which can explain the large static deflections of the proof masses in some of the devices (> 50 nm).

In summary, the built-in stresses can be explained as a result of strong van der Waals interactions between the graphene and the SiO_2 surface at the microscopically rounded edges and sidewalls of the etched trenches[6, 36]. In the case of ribbons made of single-layer graphene, this force only influences the adhesion between the edges of the graphene ribbons and the underlying SiO_2 surface while for ribbons made of double-layer graphene it influences the graphene and substrate adhesion as well as the adhesion between the graphene layers[7, 71].

S22. Spring constants of suspended graphene devices reported in literature

TABLE S15. Reported spring constants of clamped and suspended graphene devices.

Author	Year	Graphene type	Structure and dimensions (area)	Thickness (nm)	Measurement method	Spring constant (N/m)
Present work	2019	CVD	Doubly-clamped suspended graphene ribbons with attached proof mass	Double-layer (~0.67 nm)	Mechanical resonance frequency	~10^{0}
Blees[19]	2015	CVD	Graphene kirigami cantilever with pad at the end (Length: 8-80 µm, Width: 2-15 µm)	Single-layer (~0.335 nm)	Thermal fluctuations	10^{-5}-10^{-8}
Blees[19]	2015	CVD	Graphene kirigami pyramid with central pad	Single-layer (~0.335 nm)	Thermal fluctuations	10^{-6}
Shivaraman[29]	2009	Epitaxy	Doubly-clamped graphene (ribbon) (~ 4.5 µm × 1.3 µm)	Graphene sheets (1 nm)	AFM indentation	10^{-1}
					Optical resonance	10^{0}
					Standard beam theory	10^{-2}-10^{-3}
Bunch[10]	2007	Mechanical exfoliation	Doubly-clamped graphene (ribbon) (~ 2.7 µm × 0.6 µm)	Graphene sheets (5 nm)	Thermal excitation resonance	0.7
Frank[30]	2007	Mechanical exfoliation	Doubly-clamped Graphene (ribbon) (~ 3 µm × 1.2 µm)	Graphene sheets (2-8 nm)	AFM indentation	1-5

S23. Gauge factors of graphene strain gauges

TABLE S16. Gauge factors of graphene strain gauges reported in literature.

Author	Year	Graphene source	Structure type	Graphene thickness (nm)	Strain in graphene	Gauge factor of graphene
Li[78]	2016	Chemical reduction of graphene oxide	Porous structure for RGO membrane	Membrane	0% - 1%	15.2 - 46.1
Wang[79]	2016	CVD	Graphene microdrums on a freestanding perforated SiNx thin membrane	Few-layer (~ 2 nm)	0.22%	4.4
Benameur[40]	2015	Mechanical exfoliation	Doubly-clamped suspended ribbon over trench	Single-layer (0.335 nm)	5%	8.8
Young[80]	2015	CVD	Stacked multi-layered strain sensor	Single-layer (0.335 nm)	2.67%, 10%	1.4 - 2
Xu[81]	2014	Mechanical exfoliation	Doubly-clamped suspended ribbon over trench	Single-layer (0.335 nm)	0% - 0.054%	0.6
Gamil[82]	2014	Chemical reduction of graphene oxide	RGO strain gauge on a PET substrate	Multilayer film (2.5 µm)	0.01 - 0.04%	61.5
Smith[12]	2013	CVD	Suspended membrane clamped on rectangular cavity	Single-layer (0.335 nm)	0.29%	3.67
Zheng[41]	2013	Mechanical exfoliation	Graphene on silicon wafer with a strain gauge	One to five layers (0.335-1.675 nm)	0% - 0.084%	10 - 15
Zhu[39]	2013	CVD	Suspended membrane clamped on circular cavity	Multilayer graphene	~ 0.25%	1.6
Hempel[83]	2012	Spray-deposited dispersion	Percolative film on plastic substrate	Thin film	0% - 1.7%	10 - 100
Zhao[84]	2012	RPECVD	Densely packed nanographene islands	Nanographene film (one to few layers)	0% - 0.3%	0 - 325
Li[85]	2012	CVD	Graphene woven fabrics on PDMS		2% - 6%	~1000
Hosseinzadegan[86]	2012	CVD	Graphene on suspended silicon-nitride membrane	Single-layer (0.335 nm)	0% - 0.00025%	18000
Huang[42]	2011	Mechanical exfoliation	Doubly-clamped suspended ribbon over trench	Flakes (one or two layers) (0.335-0.67 nm)	~ 3%	~ 1.9
Wang[87]	2011	Mechanical exfoliation	Graphene ripples on PDMS	Single-layer (0.335 nm)	> 30%	~ 2
Kim[88]	2011	Dispersion	Graphene/epoxy composite		1000 micro-strain	11.4
Lee[89]	2010	CVD	Graphene on PDMS	Mainly one and two layers (0.335-0.67 nm)	1%	6.1

S24. Discussion of possible effects at the graphene anchor positions

It is in principle possible that interactions between the graphene ribbons and the SiO_2 surface at the trench edges (i.e. the anchoring positions of the graphene ribbons) and delamination effects contribute to the resistance changes in the graphene ribbons in our acceleration measurements. However, based on our theoretical analysis we presume that possible contributions from effects at the trench edges on the measured resistance changes in the graphene transducers are negligible. Our analysis is based on three items:

1) Koenig *et al.*[7] report that the van der Waals forces between graphene sheets and SiO_2 surfaces are extremely strong. For example, adhesion energies of 0.31 ± 0.03 J m^{-2} were measured between two to five-layer graphene and SiO_2 surfaces. In the study by Koenig *et al.*[7] the delamination of graphene from a SiO_2 substrate surface was investigated for the case of a graphene membrane that is suspended over a circular cavity with a diameter of 5 µm. Delamination of the graphene from the SiO_2 substrate was only observed if a pressure difference of more than 1.9 MPa was applied between the inside of the cavity and the outside atmosphere. Based on a rough approximation (multiplying the membrane area with the applied pressure), the corresponding critical force on the graphene membrane that caused the graphene to delaminate at the edge of the cavities can be estimated to ~ 40 µN. In contrast, the forces that act on the graphene ribbons in our devices when exposed to an acceleration of 1 g are of the order of 1 nN. While the geometric situation is not identical for both cases, the forces acting on the graphene ribbons in our devices are more than 4 orders of magnitude smaller than the forces that caused the graphene to delaminate in the circular devices in Koenig *et al.*[7]. This is a very strong indication that delamination of the graphene ribbons should not be expected in our devices.

2) The deflection of suspended graphene ribbons with an attached silicon proof mass is very small in our acceleration measurements. For example, when an acceleration of 1 g at a frequency of 160 Hz (as measured by reference accelerometer of the shaker), is applied to device 1, the deflection of the proof mass and the graphene ribbons is assumed to be at most of the order of 10 nm. For a geometric analysis of the situation at the trench edges, we assumed that the edges have rounded corners with a radius of the order of 100 nm (Figure S22). For deflections of the graphene ribbons towards the substrate (with the conservative assumption of absence of van der Waals forces), the line segment “GF” is the deflection (d) of the proof mass, the line segment “EF” is the width of the trench (l), and the line segments “OA”, “OB” and “OC” are approximated by the curve radius (r) of the trench

edge. "AC" is the length (z) of the section of the graphene ribbon that gets in contact with the SiO_2 substrate surface as a result of the graphene ribbon deflection. The length z can be approximated by

$$z \approx \sqrt{\frac{1}{(\frac{l+r}{2\,r\,d})^2 - \frac{1}{4\,r^2}}} \qquad \text{(S44)}$$

In the example of device 1 and assuming d = 10 nm, l = 3 μm and r = 100 nm, the length of the section of the graphene that contacts the SiO_2 substrate surface as a result of the ribbon deflection is of the order of 0.65 nm. This means that any small movement of the graphene with respect to the SiO_2 surface at the trench edges would affect only an extremely short section of the graphene ribbons, thus having a negligible impact on the overall resistance of the graphene ribbons in our devices.

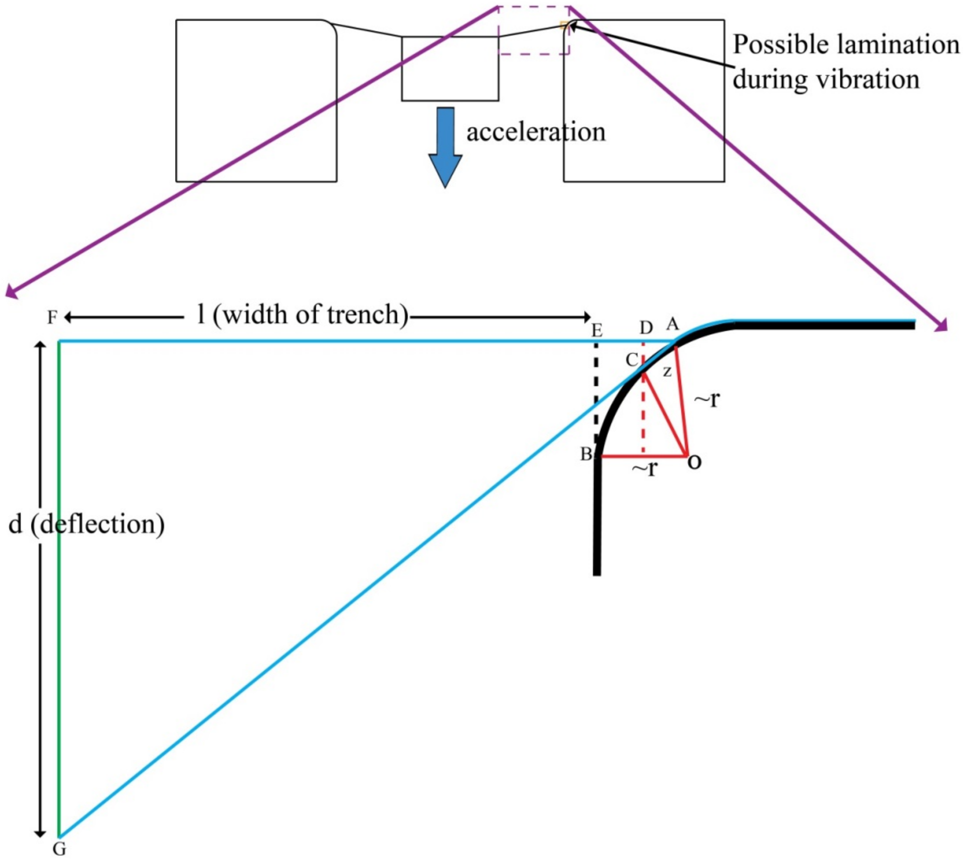

Figure S22| Schematic of the geometric situation at the trench edge, i.e. the anchor points of the graphene ribbons, when the graphene ribbons are deflected towards the substrate.

3) Kang *et al.*[90] report that the influence of a SiO_2 surface on the resistivity of double-layer graphene is much smaller as compared to the influence of a SiO_2 surface on the resistivity of single-layer graphene. This means that any small movement of the double-layer graphene ribbons relative to the SiO_2 surface at the trench edges would have only a very small impact on the resistance of the double-layer graphene ribbons in our devices.

S25. Young’s modulus of graphene-based materials

A comparison of reported Young’s modulus values of graphene-based materials is shown in the Table S17. The reported Young’s modulus values range from 0.06 TPa to 3.43 TPa, depending on the graphene type, quality, number of layers and the measurement method.

TABLE S17. Comparison of Young’s modulus values of graphene-based materials reported in literature.

Author	Year	Graphene source	Structure	Graphene thickness (nm)	Measurement method	Young’s modulus (TPa)
Present work	2019	CVD	Doubly-clamped suspended ribbons with attached proof mass	Double-layer (~ 0.67 nm)	AFM indentation	0.22 (average value)
Davidovikj[73]	2017	Mechanical exfoliation	Fully-clamped suspended membrane on circular cavity	Multi-layer graphene flake (5 nm)	AFM indentation	0.59
					Electrostatic resonance	
Nicholl[46]	2015	CVD	Fully-clamped suspended membrane on circular cavity	Single-layer (~ 0.335 nm)	Electrostatically pressured with interferometric profilometry	0.06 - 0.3
			Fully-clamped suspended membrane on circular cavity followed by being cut into a ribbon			~0.41 ± 0.026 (ribbon width: 5 μm) ~ 0.9 ± 0.15 (ribbon width: 2.7 μm)
Lopez-Polin[14]	2015	Mechanical exfoliation	Graphene drum	Single-layer (~ 0.335 nm)	AFM indentation	~ 0.75 - ~ 1.07
Lee[50]	2013	CVD	Suspended membrane clamped on circular cavity	Single-layer (~ 0.335 nm)	AFM indentation	1
Lee[91]	2012	Mechanical exfoliation	Suspended membrane clamped on circular cavity	Single-layer (~ 0.335 nm)	Raman spectroscopy	2.4 ± 0.4
				Two layers (~ 0.67 nm)	Raman spectroscopy	2 ± 0.5
				Four layers (~ 1.34 nm)	Raman spectroscopy	1.7 ± 0.5
Annamalai[71]	2012	Mechanical exfoliation	Fully-clamped suspended membrane on circular cavity	Single-layer (~ 0.335 nm)	AFM indentation	1.12
				Two layers (~ 0.67 nm)	AFM indentation	3.25
				Three layers (~ 1.34 nm)	AFM indentation	3.25
				Five layers (~ 1.675 nm)	AFM indentation	3.43

Koenig[7]	2011	Mechanical exfoliation	Suspended membrane clamped on circular cavity	One to five layers (~ 0.335 - ~ 1.675 nm)	Pressurized blister tester	~ 1
Ruiz-Vargas[23]	2011	CVD	Suspended membrane clamped on circular cavity	Single-layer (~ 0.335 nm)	AFM indentation	0.164 (average value)
Lee[6]	2008	Mechanical exfoliation	Suspended membrane clamped on circular cavity	Single-layer (~ 0.335 nm)	AFM indentation	1
Gómez-Navarro[9]	2008	Chemical reduction of graphene oxide	Doubly-clamped suspended beam over trench	Single-layer (~ 0.335 nm)	AFM indentation	0.25
Frank[30]	2007	Mechanical exfoliation	Doubly-clamped suspended beam over trench	Graphene sheets (2-8 nm)	AFM indentation	0.5
Blakslee[92]	1970	Bulk graphite			Ultrasonic, sonic resonance and static tests	1

S26. Supplementary References

1. Borgia, E. The Internet of Things vision: Key features, applications and open issues. *Comput. Commun.* **54,** 1–31 (2014).
2. del Rosario, M., Redmond, S. & Lovell, N. Tracking the evolution of smartphone sensing for monitoring human movement. *Sensors* **15,** 18901–18933 (2015).
3. Brigante, C.M.N., Abbate, N., Basile, A., Faulisi, A.C. & Sessa, S. Towards miniaturization of a MEMS-Based wearable motion capture system. *IEEE T. Ind. Electron.* **58,** 3234–3241 (2011).
4. Shasha Liu, P. & Tse, H.-F. Implantable sensors for heart failure monitoring. *J. Arrhythm.* **29,** 314–319 (2013).
5. Bolotin, K.I. et al. Ultrahigh electron mobility in suspended graphene. *Solid State Commun.* **146,** 351–355 (2008).
6. Lee, C., Wei, X., Kysar, J. W. & Hone, J. Measurement of the elastic properties and intrinsic strength of monolayer graphene. *Science* **321,** 385–388 (2008).
7. Koenig, S. P., Boddeti, N. G., Dunn, M. L. & Bunch, J. S. Ultrastrong adhesion of graphene membranes. *Nat. Nanotechnol.* **6,** 543–546 (2011).
8. Lau, C. N., Bao, W. & Velasco Jr, J. Properties of suspended graphene membranes. *Mater. Today* **15,** 238–245 (2012).
9. Gómez-Navarro, C., Burghard, M. & Kern, K. Elastic properties of chemically derived single graphene sheets. *Nano Lett.* **8,** 2045–2049 (2008).
10. Bunch, J. S. et al. Electromechanical resonators from graphene sheets. *Science* **315,** 490–493 (2007).
11. Chen C. Y. & Hone, J. Graphene nanoelectromechanical systems. *P. IEEE* **101,** 1766–1779 (2013).
12. Smith, A. D. et al. Electromechanical piezoresistive sensing in suspended graphene membranes. *Nano Lett.* **13,** 3237–3242 (2013).
13. Kumar, M. & Bhaskaran, H. Ultrasensitive room-temperature piezoresistive transduction in graphene-based nanoelectromechanical systems. *Nano Lett.* **15,** 2562–2567 (2015).
14. López-Polín, G. et al. Increasing the elastic modulus of graphene by controlled defect creation. *Nat. Phys.* **11,** 26–31 (2015).
15. López-Polín, G., et al. The influence of strain on the elastic constants of graphene. *Carbon* **124,** 42–48 (2017).
16. Neumaier, D., Pindl, S. & Lemme, M.C. Integrating graphene into semiconductor fabrication lines. *Nat. Mater.* **18,** 525 (2019).

17. Li, X. et al. Large-area synthesis of high-quality and uniform graphene films on copper foils. *Science* **324,** 1312–1314 (2009).
18. Hurst, A. M., Lee, S., Cha, W. & Hone, J. A graphene accelerometer. in *2015 28th IEEE International Conference on Micro Electro Mechanical Systems (MEMS)* 865–868 (2015).
19. Blees, M. K. et al. Graphene kirigami. *Nature* **524,** 204–207 (2015).
20. Matsui, K. et al. Mechanical properties of few layer graphene cantilever. in *2014 IEEE 27th International Conference on Micro Electro Mechanical Systems (MEMS)* 1087–1090 (2014).
21. Zhang, P. et al. Fracture toughness of graphene. *Nat. Commun.* **5,** (2014).
22. Shekhawat, A. & Ritchie, R. O. Toughness and strength of nanocrystalline graphene. *Nat. Commun.* **7,** 10546 (2016).
23. Ruiz-Vargas, C.S. et al. Softened Elastic Response and Unzipping in Chemical Vapor Deposition Graphene Membranes. *Nano Lett.* **11,** 2259–2263 (2011).
24. Chen, Z., Lin, Y.-M., Rooks, M.J. & Avouris, P. Graphene nano-ribbon electronics. *Physica E* **40,** 228–232 (2007).
25. Balandin, A.A. Low-frequency 1/f noise in graphene devices. *Nat. Nanotechnol.* **8,** 549–555 (2013).
26. Lin, Y.-M. & Avouris, P. Strong Suppression of Electrical Noise in Bilayer Graphene Nanodevices. *Nano Lett.* **8,** 2119–2125 (2008).
27. Kavitha, S., Daniel, R.J. & Sumangala, K. A simple analytical design approach based on computer aided analysis of bulk micromachined piezoresistive MEMS accelerometer for concrete SHM applications. *Measurement* **46,** 3372–3388 (2013).
28. Lynch J.P. et al. Design of Piezoresistive MEMS-Based Accelerometer for Integration with Wireless Sensing Unit for Structural Monitoring. *J. Aerospace Eng.* **16,** 108–114 (2003).
29. Shivaraman, S. et al. Free-standing epitaxial graphene. *Nano Lett.* **9,** 3100–3105 (2009).
30. Frank, I.W., Tanenbaum, D.M., Zande, A.M. van der & McEuen, P.L. Mechanical properties of suspended graphene sheets. *J. Vac. Sci. Technol. B Nanotechnol. Microelectron.* **25,** 2558–2561 (2007).
31. Senturia, S.D. *Microsystem Design Ch.10* (Kluwer Academic, New York, Boston, Dordrecht, London, Moscow, 2002).
32. Castellanos-Gomez, A., Singh, V., van der Zant, H.S.J. & Steele, G.A. Mechanics of freely-suspended ultrathin layered materials: Mechanics of 2D materials. *Ann. Phys-Berlin* **527,** 27–44 (2015).

33. Traversi, F., et al. Elastic properties of graphene suspended on a polymer substrate by e-beam exposure. *New J. Phys.* **12,** 023034 (2010).
34. Li, P., You, Z., Haugstad, G. & Cui, T. Graphene fixed-end beam arrays based on mechanical exfoliation. *Appl. Phys. Lett.* **98,** 253105 (2011).
35. Li, Y., Zheng, Q., Hu, Y. & Xu, Y. Micromachined Piezoresistive Accelerometers Based on an Asymmetrically Gapped Cantilever. *J. Microelectromech. S.* **20,** 83–94 (2011).
36. Bunch, J.S. et al. Impermeable Atomic Membranes from Graphene Sheets. *Nano Lett.* **8,** 2458–2462 (2008).
37. Garcia-Sanchez, D. et al. Imaging Mechanical Vibrations in Suspended Graphene Sheets. *Nano Lett.* **8,** 1399–1403 (2008).
38. Yazdi, N., Ayazi, F. & Najafi, K. Micromachined inertial sensors. *P. IEEE* **86,** 1640–1659 (1998).
39. Zhu, S.-E., Ghatkesar, M.K., Zhang, C. & Janssen, G. Graphene based piezoresistive pressure sensor. *Appl. Phys. Lett.* **102,** 161904 (2013).
40. Benameur, M.M. et al. Electromechanical oscillations in bilayer graphene. *Nat. Commun.* **6,** 8582 (2015).
41. Zheng, X., Chen, X., Kim, J.-K., Lee, D.-W. & Li, X. Measurement of the gauge factor of few-layer graphene. *J. Micro-nanolith Mem.* **12,** 013009–013009 (2013).
42. Huang, M., Pascal, T.A., Kim, H., Goddard, W.A. & Greer, J.R. Electronic-mechanical coupling in graphene from in situ nanoindentation experiments and multiscale atomistic simulations. *Nano Lett.* **11,** 1241–1246 (2011).
43. Nicholl, R.J.T., et al. The effect of intrinsic crumpling on the mechanics of free-standing graphene. *Nat. Commun.* **6,** (2015).
44. Wung, T.-S., Ning, Y.-T., Chang, K.-H., Tang, S. & Tsai, Y.-X. Vertical-plate-type microaccelerometer with high linearity and low cross-axis sensitivity. *Sensor Actuat. A-Phys.* **222,** 284–292 (2015).
45. Fischer, A.C. et al. Integrating MEMS and ICs. *Microsyst. Nanoeng.* **1,** 15005 (2015).
46. Roy, A.L. & Bhattacharyya, T. K. Design, fabrication and characterization of high performance SOI MEMS piezoresistive accelerometers. *Microsyst. Technol.* **21,** 55–63 (2015).
47. Zhang, L., Lu, J., Kurashima, Y., Takagi, H. & Maeda, R. Development and application of planar piezoresistive vibration sensor. *Microelectron. Eng.* **119,** 70–74 (2014).
48. Plaza, J.A., Collado, A., Cabruja, E. & Esteve, J. Piezoresistive accelerometers for MCM package. *J. Microelectromech. S.* **11,** 794–801 (2002).

49. Manzeli, S., Allain, A., Ghadimi, A. & Kis, A. Piezoresistivity and Strain-induced Band Gap Tuning in Atomically Thin MoS_2. *Nano Lett.* **15,** 5330–5335 (2015).
50. Lee, G.-H. et al. High-strength chemical-vapor–deposited graphene and grain boundaries. *Science* **340,** 1073–1076 (2013).
51. Salvetat, J.-P. et al. Elastic and shear moduli of single-walled carbon nanotube ropes. *Phys. Rev. Lett.* **82,** 944 (1999).
52. Zandiatashbar, A., et al. Effect of defects on the intrinsic strength and stiffness of graphene. *Nat. Commun.* **5,** (2014).
53. Han, J., Ryu, S., Kim, D.-K., Woo, W. & Sohn, D. Effect of interlayer sliding on the estimation of elastic modulus of multilayer graphene in nanoindentation simulation. *EPL* **114**, 68001 (2016).
54. Wei, X. et al. Recoverable Slippage Mechanism in Multilayer Graphene Leads to Repeatable Energy Dissipation. *ACS Nano* **10**, 1820–1828 (2016).
55. Nicholl, R. J. T., Lavrik, N. V., Vlassiouk, I., Srijanto, B. R. & Bolotin, K. I. Hidden Area and Mechanical Nonlinearities in Freestanding Graphene. *Phys. Rev. Lett.* **118,** (2017).
56. Fan, X. et al. Direct observation of grain boundaries in graphene through vapor hydrofluoric acid (VHF) exposure. *Sci. Adv.* **4**, eaar5170 (2018).
57. Smith, A.D., Vaziri, S., Rodriguez, S., Östling, M. & Lemme, M.C. Large scale integration of graphene transistors for potential applications in the back end of the line. *Solid State Electron.* **108,** 61–66 (2015).
58. Wagner, S. et al. Graphene transfer methods for the fabrication of membrane-based NEMS devices. *Microelectron. Eng.* **159,** 108–113 (2016).
59. Kavitha, S., Joseph Daniel, R. & Sumangala, K. High performance MEMS accelerometers for concrete SHM applications and comparison with COTS accelerometers. *Mech. Syst. Signal Pr.* **66-67,** 410–424 (2016).
60. Roy, A.L., Sarkar, H., Dutta, A. & Bhattacharyya, T.K. A high precision SOI MEMS–CMOS ±4g piezoresistive accelerometer. *Sensor Actuat. A-Phys.* **210,** 77–85 (2014).
61. Haris, M. & Qu, H. A CMOS-MEMS piezoresistive accelerometer with large proof mass. in Nano/Micro Engineered and Molecular Systems (NEMS), 2010 5th IEEE International Conference on 309–312 (IEEE, 2010).
62. Kal, S. et al. CMOS compatible bulk micromachined silicon piezoresistive accelerometer with low off-axis sensitivity. *Microelectron. J.* **37,** 22–30 (2006).

63. Ma, M. A combined modulated feedback and temperature compensation approach to improve bias drift of a closed-loop MEMS capacitive accelerometer. *Front. Inform. Tech. El.* **16,** 497–510 (2015).
64. Chae, J., Kulah, H. & Najafi, K. A monolithic three-axis micro-g micromachined silicon capacitive accelerometer. *J. Microelectromech. S.* **14,** 235–242 (2005).
65. Zhou, W. et al. Air damping analysis in comb microaccelerometer. *Adv. Mech. Eng.* **6,** 373172 (2014).
66. Aydin, O. & Akin, T. A bulk-micromachined fully differential MEMS accelerometer with split interdigitated fingers. *IEEE Sens. J.* **13,** 2914–2921 (2013).
67. Sun, H. et al. A low-power low-noise dual-chopper amplifier for capacitive CMOS-MEMS accelerometers. *IEEE Sens. J.* **11,** 925–933 (2011).
68. Amini, B.V. & Ayazi, F. A 2.5-V 14-bit /spl Sigma//spl Delta/ CMOS SOI capacitive accelerometer. *IEEE J. Solid-st Circ.* **39,** 2467–2476 (2004).
69. Low Frequency Magnetic Shielding – An Integrated Solution, Integran Technologies Inc.
70. Sansa, M., Fernández-Regúlez, M., Llobet, J., San Paulo, Á. & Pérez-Murano, F. High-sensitivity linear piezoresistive transduction for nanomechanical beam resonators. *Nat. Commun.* **5**, 4313 (2014).
71. Annamalai, M., Mathew, S., Jamali, M., Zhan, D. & Palaniapan, M. Elastic and nonlinear response of nanomechanical graphene devices. *J. Micromech. Microeng.* **22,** 105024 (2012).
72. Poot, M. & van der Zant, H. S. J. Nanomechanical properties of few-layer graphene membranes. *Appl. Phys. Lett.* **92,** 063111 (2008).
73. Davidovikj, D. et al. Nonlinear dynamic characterization of two-dimensional materials. *Nat. Commun.* **8,** 1253 (2017).
74. Patel, R.N., Mathew, J.P., Borah, A. & Deshmukh, M.M. Low tension graphene drums for electromechanical pressure sensing. *2D Mater.* **3,** 011003 (2016).
75. Lee, S. et al. Electrically integrated SU-8 clamped graphene drum resonators for strain engineering. *Appl. Phys. Lett.* **102,** 153101 (2013).
76. Zande, A. M. van der et al. Large-scale arrays of single-layer graphene resonators. *Nano Lett.* **10,** 4869–4873 (2010).
77. Chen, C. et al. Performance of monolayer graphene nanomechanical resonators with electrical readout. *Nat. Nanotechnol.* **4,** 861–867 (2009).
78. Li, J.-C., Weng, C.-H., Tsai, F.-C., Shih, W.-P. & Chang, P.-Z. Porous reduced graphene

oxide membrane with enhanced gauge factor. *Appl. Phys. Lett.* **108,** 013108 (2016).

79. Wang, Q., Hong, W. & Dong, L. Graphene 'microdrums' on a freestanding perforated thin membrane for high sensitivity MEMS pressure sensors. *Nanoscale* **8,** 7663–7671 (2016).
80. Young, C. MEMS graphene strain sensor. *Graduate Theses and Dissertations*, Iowa State University, (2015).
81. Xu, K. et al. The positive piezoconductive effect in graphene. *Nat. Commun.* **6,** 8119 (2015).
82. Gamil, M. et al. Graphene-based strain gauge on a flexible substrate. *Sens. Mater.* **26,** 699–709 (2014).
83. Hempel, M., Nezich, D., Kong, J. & Hofmann, M. A novel class of strain gauges based on layered percolative films of 2D materials. *Nano Lett.* **12,** 5714–5718 (2012).
84. Zhao, J. et al. Ultra-sensitive strain sensors based on piezoresistive nanographene films. *Appl. Phys. Lett.* **101,** 063112 (2012).
85. Li, X. et al. Stretchable and highly sensitive graphene-on-polymer strain sensors. *Sci. Rep.* **2,** (2012).
86. Hosseinzadegan, H. et al. Graphene has ultrahigh piezoresistive gauge factor. in *Micro Electro Mechanical Systems (MEMS), 2012 IEEE 25th International Conference on* 611–614 (IEEE, 2012).
87. Wang, Y. et al. Super-Elastic Graphene ripples for flexible strain sensors. *ACS Nano* **5,** 3645–3650 (2011).
88. Kim, Y.-J. et al. Preparation of piezoresistive nano smart hybrid material based on graphene. *Curr. Appl. Phys.* **11,** S350–S352 (2011).
89. Lee, Y. et al. Wafer-scale synthesis and transfer of graphene films. *Nano Lett.* **10,** 490–493 (2010).
90. Kang, Y.-J., Kang, J. & Chang, K. J. Electronic structure of graphene and doping effect on SiO_2. *Phys. Rev. B* **78,** (2008).
91. Lee, J.-U., Yoon, D. & Cheong, H. Estimation of Young's modulus of graphene by Raman spectroscopy. *Nano Lett.* **12,** 4444–4448 (2012).
92. Blakslee, O. L., Proctor, D. G., Seldin, E. J., Spence, G. B. & Weng, T. Elastic constants of compression-annealed pyrolytic graphite. *J. Appl. Phys.* **41,** 3373–3382 (1970).